

# Global Representations of Goal-Directed Behavior in Distinct Cell Types of Mouse Neocortex

## Highlights

- Large-scale two-photon and wide-field imaging across cortex during behavior
- Cells and neuropil throughout cortex exhibit task-related activity
- Different types of neurons exhibit specific cortex-wide activity dynamics
- This cortex-wide activity pattern depends specifically on premotor cortex

## Authors

William E. Allen, Isaac V. Kauvar,  
Michael Z. Chen, ...,  
Benjamin E. Deverman, Liqun Luo,  
Karl Deisseroth

## Correspondence

lluo@stanford.edu (L.L.),  
deissero@stanford.edu (K.D.)

## In Brief

Allen et al. combine two-photon and wide-field imaging with transgenic GCaMP expression to survey activity in several molecularly defined cell types across the cortex of mice performing a decision-making task and discover widespread task-related activity that is gated by premotor cortex.

# Global Representations of Goal-Directed Behavior in Distinct Cell Types of Mouse Neocortex

William E. Allen,<sup>1,3,4,8</sup> Isaac V. Kauvar,<sup>2,4,8</sup> Michael Z. Chen,<sup>4</sup> Ethan B. Richman,<sup>1,3,4</sup> Samuel J. Yang,<sup>2,4</sup> Ken Chan,<sup>7</sup> Viviana Gradinaru,<sup>7</sup> Benjamin E. Deverman,<sup>7</sup> Liqun Luo,<sup>3,5,\*</sup> and Karl Deisseroth<sup>4,5,6,9,\*</sup>

<sup>1</sup>Neurosciences Graduate Program

<sup>2</sup>Electrical Engineering Graduate Program

<sup>3</sup>Department of Biology

<sup>4</sup>Department of Bioengineering

<sup>5</sup>Howard Hughes Medical Institute

<sup>6</sup>Department of Psychiatry and Behavioral Sciences

Stanford University, Stanford, CA 94305, USA

<sup>7</sup>Division of Biology and Bioengineering, California Institute of Technology, Pasadena, CA 91125, USA

<sup>8</sup>These authors contributed equally

<sup>9</sup>Lead Contact

\*Correspondence: lluo@stanford.edu (L.L.), deissero@stanford.edu (K.D.)

<http://dx.doi.org/10.1016/j.neuron.2017.04.017>

## SUMMARY

The successful planning and execution of adaptive behaviors in mammals may require long-range coordination of neural networks throughout cerebral cortex. The neuronal implementation of signals that could orchestrate cortex-wide activity remains unclear. Here, we develop and apply methods for cortex-wide  $\text{Ca}^{2+}$  imaging in mice performing decision-making behavior and identify a global cortical representation of task engagement encoded in the activity dynamics of both single cells and superficial neuropil distributed across the majority of dorsal cortex. The activity of multiple molecularly defined cell types was found to reflect this representation with type-specific dynamics. Focal optogenetic inhibition tiled across cortex revealed a crucial role for frontal cortex in triggering this cortex-wide phenomenon; local inhibition of this region blocked both the cortex-wide response to task-initiating cues and the voluntary behavior. These findings reveal cell-type-specific processes in cortex for globally representing goal-directed behavior and identify a major cortical node that gates the global broadcast of task-related information.

## INTRODUCTION

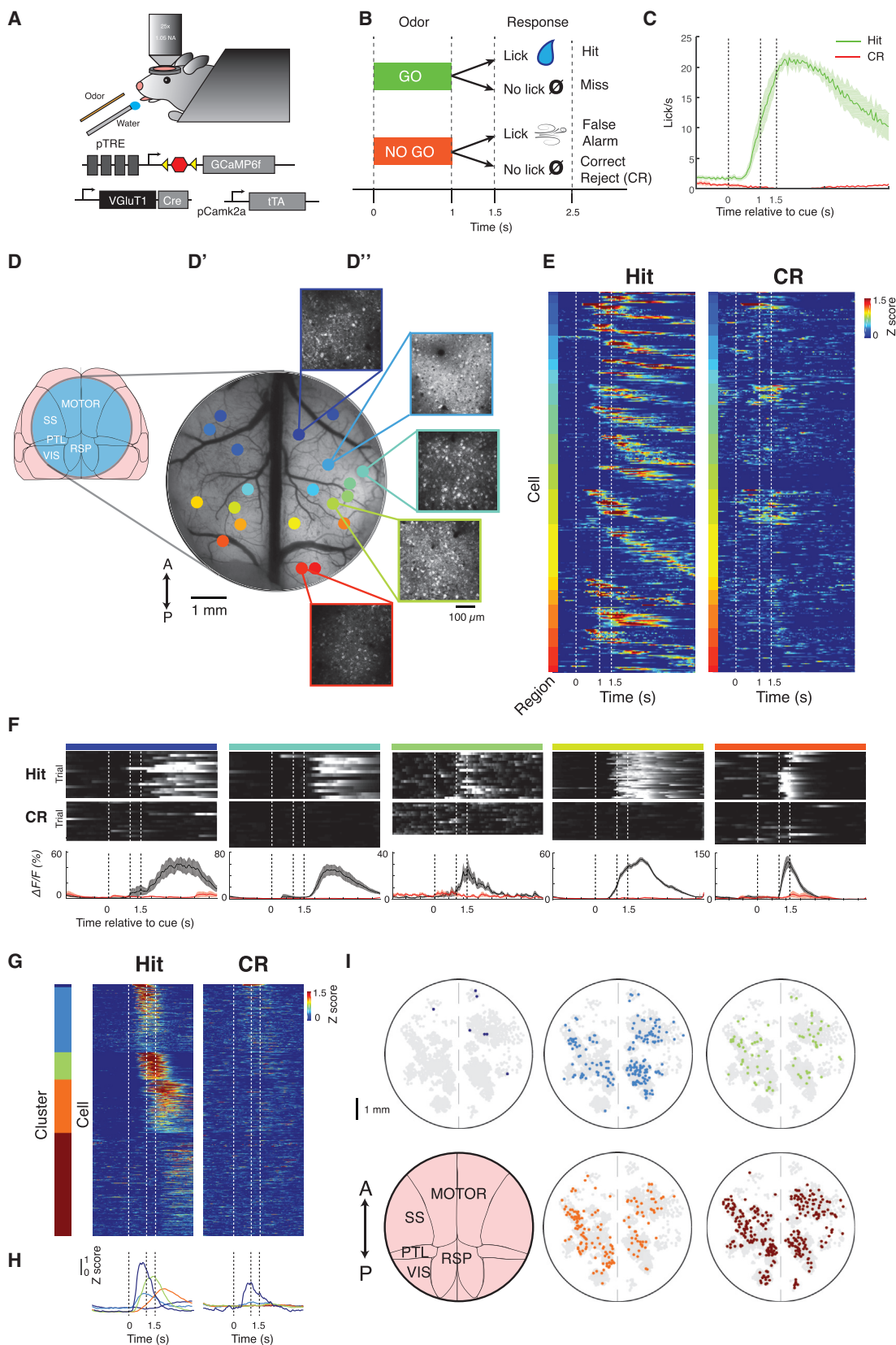
Adaptive, goal-directed behaviors are crucial for animals to survive in changing environments. These behaviors require animals to integrate immediate stimuli, internal state, and past experience in order to rapidly and flexibly select specific actions toward a particular goal. It is thought that the production of such coordinated behaviors may require the organization of neuronal activity within disparate sensory, motor, and state-regulation

systems in the brain, implemented in distinct interconnected neural circuits (Swanson, 2000). In mammals, the neocortex is commonly associated with the production of learned, adaptive forms of goal-directed behaviors, and its evolutionary expansion correlates with, and appears to underlie, some of the advanced cognitive abilities of human beings and other primates (Harris and Mrsic-Flogel, 2013; Huang and Zeng, 2013). However, the extent to which, and mechanisms by which, neural activity is coordinated across cortex to produce a single unified behavioral output remain incompletely understood.

Recent experimental data and theories suggest an important role for dynamic, reciprocal interactions in coordinating activity across different cortical areas to produce voluntary behavior and cognition (Cisek and Kalaska, 2010; Engel et al., 2001; Gilbert and Li, 2013; Miller and Cohen, 2001). Extensive theoretical and experimental analysis has described how these recurrent interactions may produce complex spatial and temporal patterns of activity, both spontaneously and in response to specific inputs (Douglas and Martin, 2007; Yuste, 2015). Simple sensorimotor tasks can involve extensive cortical activation and changes in spike synchrony and coherence (Engel et al., 2001; Roelfsema et al., 1997). During goal-directed behavior, interactions between different cortical areas are thought, in part, to allow “top-down,” task-related information—such as expectations, decisions, rules, goals, or outcomes that derive from experience—to play a role in modulating local computations to guide behavior. In particular, feedback projections from multimodal association areas carrying this information have been proposed to actively control the flow of information in cortex in a flexible manner (Buschman and Miller, 2007; Miller and Cohen, 2001).

Although indirect evidence from both rodents and nonhuman primates hints at the existence of widespread task-related signals, the majority of studies surveying different cortical regions during goal-directed behavior have focused primarily on identifying region-specific patterns of activity that could explain local computations (Goard et al., 2016; Hernández et al., 2010; Ledberg et al., 2007; Poort et al., 2015; Siegel et al., 2015). These pioneering studies typically investigated areas believed a priori





(legend on next page)

to be involved in a behavior, leaving unresolved the question of whether activity is coordinated throughout the whole cortex or just in specific pathways. Furthermore, these important studies are primarily correlative, leaving it unclear which parts of the cortex, if any, are responsible for orchestrating cortical activity. Finally, these studies necessarily left unaddressed distinctions between cell types, although recent studies reporting task-related activity in inhibitory interneurons in single cortical areas have suggested distinct roles for different types of interneurons in representing behavioral state information (Peron et al., 2015; Pinto and Dan, 2015). Thus, despite its potential importance for the performance of goal-directed behavior, the cellular and circuit implementation of global task-related signals, as well as the role of individual cortical regions in gating this widespread activity, remain largely unexplored.

To explore biological mechanisms underlying the coordination of cortical activity during behavior, we set up an experimental paradigm designed to address several key questions: (1) Does goal-directed behavior produce a globally distributed cortical state representing task information such as decisions or expectations, or is this representation restricted to specific regions of cortex necessary for a behavior? (2) Is this state similarly represented in different cell types, or do some cell types favor local computations while others represent the behavioral state? (3) Can single cortical regions act as hubs that are necessary for the generation of this state?

To answer these questions, we sought to bridge the gap between single-cell coding and global brain dynamics by broadly surveying neocortical activity during behavior. In awake, behaving mice performing an olfactory go/no-go decision-making task, we used tiled two-photon imaging to investigate local single-cell coding across the cortex and developed a technique for whole-cortex wide-field  $\text{Ca}^{2+}$  imaging to comprehensively and synchronously record network-scale activity with cell-type specificity. We further combined wide-field imaging with pharmacological and optogenetic manipulations of behavior to examine the role of single cortical regions in the production of widespread task-related activity. Our findings reveal that apparently local patterns of activity in cortex are in fact globally coor-

dinated; that this representation is shared across many areas, but with distinct patterns in specific cell types; and that a single cortical region is necessary both for the behavior and for these globally coordinated dynamics.

## RESULTS

### Distributed Cellular Representation of Goal-Directed Task Engagement

In order to broadly survey cortical activity during a simple goal-directed behavior, we performed tiled two-photon  $\text{Ca}^{2+}$  imaging of mice performing an olfactory go/no-go decision-making task (Komiyama et al., 2010) (Figure 1A). Performance of this task is known to depend upon both motor and premotor regions that individually exhibit complex activity patterns during behavior but is not thought to rely upon any sensory cortical areas in dorsal cortex. Water-restricted mice were trained to make a behavioral decision discriminating between two odors: to lick in response to one odor (ethyl acetate) for a water reward (hit) and withhold licking to another other odor (2-pentanone) (correct reject [CR]) to avoid an aversive air puff to the rostrum (Figures 1B and 1C). Mice were imaged after reaching criterion performance of >70% correct ( $92\% \pm 9\%$  correct trials per session with  $86\% \pm 2\%$  correct rejections across 79 sessions, mean  $\pm$  SEM).

We combined a large chronic craniotomy with transgenic  $\text{Ca}^{2+}$  sensor expression to survey activity in different parts of cortex during behavior. We expressed GCaMP6f, a fast and sensitive fluorescent  $\text{Ca}^{2+}$  sensor (Chen et al., 2013b), in VGlut1<sup>+</sup> excitatory neurons throughout neocortex using a triple-transgenic strategy (Figure 1A; STAR Methods). We then exposed dorsal neocortex, spanning motor, somatosensory, parietal, and visual cortex through a 7 mm window for two-photon  $\text{Ca}^{2+}$  imaging (Figures 1D–1D'). This preparation included access to both the anatomically described somatomotor and medial sensory networks (Zingg et al., 2014). Neurons across cortex were imaged over many behavioral sessions, and a wide-field calibration image recorded each day was used to register the location of each field of view within the same reference frame. Thus, over multiple sessions, we could record thousands of superficial layer

### Figure 1. Distributed Cellular Representation of Goal-Directed Behavior

- (A) Diagram of two-photon imaging and behavioral setup and triple-transgenic strategy for tTA-amplified expression of GCaMP6f in VGlut1<sup>+</sup> excitatory neurons throughout the brain.
- (B) Diagram of olfactory discrimination task structure. Odor is delivered for 1 s, followed by 0.5 s of no stimulus, then a 1 s response window.
- (C) Average licking behavior during task performance across  $n = 4$  mice on hit (green) and correct reject (CR) (red) trials.
- (D) Surgical preparation to record single-cell activity from across cortex.
- (D') Wide-field fluorescent image through a 7 mm window that is used to expose the dorsal cortex for two-photon imaging. Different colored dots represent different fields of view acquired sequentially in different sessions (~30 trials/session).
- (D'') Insets show the maximum projection of fluorescence from single fields of view in layer 2/3 within the window, acquired with two-photon microscopy.
- (E) The average, Z-scored activity of single task-modulated neurons throughout multiple fields of view in a single mouse, ordered first according to anterior/posterior position of the field of view, then according to peak timing within each field of view. Dashed lines indicate trial events.
- (F) Examples of single neurons in fields of view ordered from anterior to posterior exhibiting reliable task-related activity on go trials. Top two rows: fluorescence of each neuron on single hit or CR trials (using scale from bottom row). Scale is same as bottom row from black to white. Bottom row: average fluorescence across hit (black) or CR (red) trials. Dashed lines indicate trial events. Mean  $\pm$  SEM.
- (G) Unsupervised clustering of average single-cell activity throughout cortex: average Z-scored fluorescence from  $n = 731$  task-modulated neurons, combining cells from  $n = 4$  animals, clustered into five groups.
- (H) Average traces of each cluster in (G) on hit and CR, color-coded according to cluster identity.
- (I) Spatial distribution throughout cortex of cells with different activity profiles: the spatial location of cells from all sessions, co-registered into a common reference space and colored according to cluster identity given the clustering in (G). Spots that are gray are cells not in that cluster.

2/3 (L2/3) cortical neurons from a single animal across millimeters of cortex, with all recordings time-aligned relative to the task (maximum projection from representative fields of view shown in **Figure 1D'**; example individual cellular traces from two fields of view shown in **Figure S1A**).

Surprisingly, individual L2/3 neurons in the majority of fields of view across cortex (31% of total recorded neurons across 70 of 79 sessions,  $n = 4$  mice) often exhibited activity on hit trials that peaked, on average, during a specific point during the trial (**Figure 1E**; example data set of average trace for all task-responsive cells from one mouse, in which color code indicates field-of-view locations according to **Figure 1D'**). The average activity of cells within every region spanned the duration of the task, but with some neurons responding only during the cue and others only after the reward period (**Figure 1E**). Moreover, the activity of each cell often qualitatively appeared reliable on average across multiple trials (**Figure 1F**; example trials for single cells from various locations across the window specified by color code in **Figure 1D'**; further example traces on single go and no-go trials in **Figure S1B**).

To characterize the heterogeneity in cellular response types, we applied hierarchical clustering to each cell's average activity pattern. The cells separated into five groups, which accurately represented our qualitatively observed distinctions in neural activity (**Figure 1G; STAR Methods**); averaging the activity traces from cells in each cluster revealed that the clusters collectively tiled the duration of the task from odor cue until the end of the trial (**Figure 1H**). Cells from four of five clusters were consistently activated only on hit trials, whereas a few cells in the remaining cluster (dark blue) were activated on both hit and CR trials (**Figures 1G and 1H**). These signals did not solely reflect the motor or sensory aspects of the licking action itself, because the majority of cells peaked in activity during the cue or reward periods (**Figures 1G and 1H**), despite the licking behavior peaking later and continuing for several seconds afterward (**Figure 1C**). Mapping the locations of cells assigned to each cluster across co-registered windows from each mouse revealed that cells from these clusters were distributed throughout cortex without any apparent spatial ordering (**Figure 1I**). This widespread distribution revealed that cells throughout cortex, including in primary sensory cortices such as somatosensory cortex, were entrained to all phases of a remarkably globally coordinated brain state during goal-directed behavior.

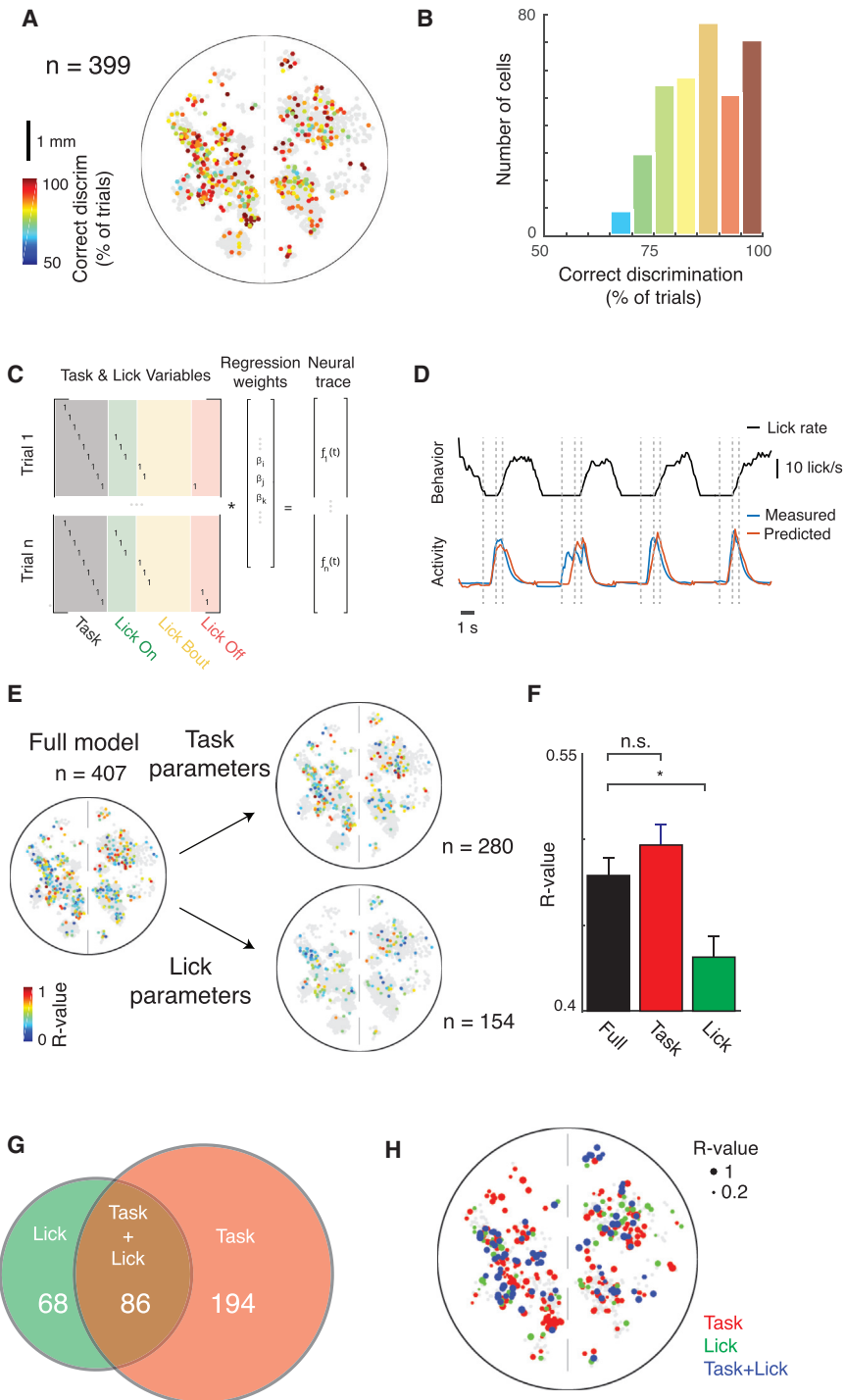
### Widespread Single-Trial Encoding of Behavioral Choice throughout Neocortex

Although the mean activity across trials in **Figure 1** is useful in describing the patterns of activity throughout cortex, we sought to examine how reliably single cells were activated during the task by quantifying how each cell encoded behavioral choice on a single-trial basis. We therefore analyzed the ability of single neurons to discriminate trial types (hit versus CR) on a trial-by-trial basis using ROC (receiver operating characteristic) analysis. We found that an ideal observer could discriminate between trial types significantly above chance levels in roughly half ( $n = 399$ ) of task-modulated neurons, again surprisingly distributed fully throughout the observable cortex with no apparent pattern ( $p < 0.05$ , permutation test) (**Figure 2A**). Neurons that could accu-

rately discriminate trial types above chance level performed well, with more than half getting >85% of individual trials correct (**Figure 2B**). Thus, individual neurons throughout cortex exhibit reliable activity that can accurately signal task engagement following odor discrimination on single trials.

In order to identify signals reflecting internal states, we next sought to further discriminate between activity related to sensorimotor feedback from the licking behavior and activity related to the animal's engagement in the task, which could indicate internal signals such as the decision to lick and expectation of reward. Because well-trained animals tend to lick immediately upon olfactory detection of the go cue, it was not possible to discriminate specific task epochs with licking-induced versus internal state-induced neuronal activity. Rather, in order to distinguish between task-responsive versus licking-responsive neurons, we determined how well neural activity could be predicted by task events versus directly measured licking behavior. Specifically, we built a generalized linear model (GLM) that sought to predict neural activity from parameters separately representing each 100 ms time window in the task from cue onward (fixed across trials) versus the onset, offset, and duration of individual lick bouts (variable across trials) (Pinto and Dan, 2015). To fit the model, a per-trial parameter matrix was constructed that had consistent indicator variables for task time points and indicator variables that represented trial-by-trial variation in the licking behavior (**Figure 2C**). Correlation between observed and predicted time series on held-out data was used to evaluate model fit (**Figure 2D**).

We then predicted each cell's activity using the full model, or using either the task or licking parameters individually, to determine if that neuron's activity was more related to the voluntary licking behavior ("licking correlated") or to the task events ("task correlated") (**Figure 2E**). Although the task and licking parameter sets differed in number, potential issues due to overfitting of a larger number of parameters were addressed by first fitting on training data and then predicting activity on a separate test data set. We found that more cells were significantly more predictive using the full set of parameters than using either just the lick or task parameters (407 cells using full parameters, 154 using lick parameters, 280 using task parameters), indicating that many neurons jointly encoded task- and licking-related information. Both licking- and task-correlated neurons were distributed throughout cortex without apparent spatial clustering (**Figure 2E**). However, among those neurons that were significantly predictive for each parameter set, the average model performance was comparable between predictions using the full parameters versus just task parameters ( $R = 0.48$  versus  $R = 0.50$ ,  $p > 0.05$ , Wilcoxon rank-sum test), whereas licking was significantly less predictive than either ( $R = 0.43$ ,  $p < 0.05$ , Wilcoxon rank-sum test) (**Figure 2F**). Under the assumptions of the GLM, cortical neurons therefore encode less information regarding the action itself, in terms of both predictive accuracy per cell and total number of active cells, than regarding task events. Fewer than half (68 of 154) of the licking-correlated cells were licking specific, whereas the majority (194 of 280) of task-correlated cells were task specific, as defined by cells that were significantly predictive using only one parameter set but not the other; 86 neurons were significant with both parameters (**Figure 2G**).

**Figure 2. Widespread Single-Trial Encoding of Behavioral Choice throughout Neocortex**

(A) Decoding of trial type on a trial-by-trial basis: spatial distribution of single cells ( $n = 399$ ) colored according to the percentage correctly distinguished single trials, as determined using ROC analysis. Non-gray cells can distinguish trial types significantly better than chance ( $p < 0.05$ , permutation test with chance level determined by shuffling trial labels).

(B) Histogram of data in (A).

(C) Structure of a generalized linear model (GLM) for separating task- and lick-related elements of neural activity. Task variables are consistent across multiple trials, whereas lick variables vary on a trial-by-trial basis.

(D) Example behavior trace (licking) and measured and GLM-predicted neural activity traces for example cell, on held out test data of four trials. Dashed lines indicated task events.

(E) Correlation of predicted and measured activity for single cells across cortex on held out test data, predicted using either the full model or just lick or task parameters in the model.  $n = 407$  cells were significantly predicted with the full model,  $n = 280$  with the task parameters, and  $n = 154$  with the lick parameters. Only cells with statistically significant predictions are shown on a background of gray non-significant cells ( $p < 0.05$ , permutation test).

(F) Average correlation coefficients for predictions using either the full model parameters, or just the licking- or task-related parameters. Same cells as in (E). \* $p < 0.05$ , Wilcoxon rank-sum test. Mean  $\pm$  SEM.

(G) Venn diagram of task- and lick-correlated cells in (E).

(H) Locations of cells throughout cortex colored by whether they are significantly predictive using the task, licking, or both task and licking parameters, with the size of each dot scaled according to the correlation between predicted and measured fluorescence using the full parameter set.

Licking-specific, task-specific, or mixed-selectivity neurons were intermingled throughout cortex (Figure 2H). Thus, according to the GLM, activity of single cells is typically more related to general task engagement state than to the specific timing of behavioral output and associated sensorimotor feedback.

This finding does not exclude the possibility that denser sampling of neural activity could reveal finer grained differences in

the fraction of cells encoding different parts of the task (Goard et al., 2016) but does show that cells throughout cortex similarly encode task engagement following behavioral choice and that this encoding is not primarily a product of sensorimotor feedback. Many cells are reliably active at specific times during the task, particularly between the cue and reward period, and are not specifically correlated with the behavioral output. This distributed activity is consistent with a model in which cellular activity patterns in cortex reflect dynamic, global brain states produced during goal-directed behavior. However, these observations were pieced together from many local observations sampling relatively small numbers of single cells asynchronously in different fields of view, only from the area accessible under a 7 mm window, and only from excitatory neurons.

## Cell-Type-Specific Cortex-wide Imaging of Neural Activity

In order to more comprehensively and synchronously survey cortical activity in different cell types, we developed a technique for truly synchronous wide-field activity recording from genetically specified neurons across the entire intact cortex of behaving animals. This approach used the combination of optics sensitive enough to record faint fluorescence signals at high speed while spanning large areas, a surgical preparation enabling chronic wide-field transcranial imaging, and genetic tools for expressing  $\text{Ca}^{2+}$  indicators in specific subsets of neurons throughout the cortex.

We began by constructing a wide-field fluorescence macroscope with highly efficient light collection and an exceptionally large 12 mm diameter field of view (Ratzlaff and Grinvald, 1991) (Figure 3A), as with concurrent approaches using wide-field imaging to examine spontaneous and sensory-evoked pan-cortical activity (Ma et al., 2016; Wekselblatt et al., 2016; Xiao et al., 2017). Distinct from these previous studies, we achieved cell-type specificity by combining Gad2-Cre and VGlut1-Cre transgenic mouse lines that express Cre recombinase in the vast majority of inhibitory GABAergic or excitatory glutamatergic (respectively) cortical neurons with high-expressing transgenic GCaMP6f Cre-reporter mice (Madisen et al., 2015) (Figures 3B and 3C). We next exposed and made transparent the intact, un-thinned skull by treatment with a clear acrylic cap, and focused the macroscope below superficial blood vessels (Guo et al., 2014) (Figure 3D). Because the macroscope does not perform optical sectioning, the transcranial fluorescence signal reflects fluorescence integrated vertically over the cortical volume, allowing collection of signals from across the cortex despite its curvature. To assign spatial localization of neural signals and register activity across different mice, we aligned each activity time series to a common reference derived from the Allen Brain Atlas (Oh et al., 2014) (Figure 3E).

We encountered a major challenge, in that even control Thy1-GFP mice (with fluorescence not expected to be responsive to neuronal  $\text{Ca}^{2+}$  levels) exhibited time-varying fluorescence signals, likely because of intrinsic autofluorescence, blood flow, and changes in blood oxygenation levels (Pisauro et al., 2013). We therefore developed a fluorescence normalization scheme on the basis of wavelength multiplexing to mitigate the influence of this artifactual signal, taking advantage of the fact that GCaMP fluorescence is effectively  $\text{Ca}^{2+}$  independent at 410 nm but  $\text{Ca}^{2+}$  dependent at 488 nm (Lerner et al., 2015) (Figures 3F and S2A). This approach allowed us to nearly simultaneously record one fluorescence video representing the neural activity plus artifacts and one video representing just the artifacts. The purely  $\text{Ca}^{2+}$ -independent signal could be subtracted from the combined signal to yield just  $\text{Ca}^{2+}$ -dependent changes in fluorescence. Control experiments in Thy1-GFP mice revealed a noise floor of <1%  $\Delta F/F$  after normalization (Figure S2E; for further methodological detail, see Figures S2A–S2G).

To validate that wide-field imaging could reproduce expected cortical activity patterns, we tested auditory stimuli (15 kHz tone, 0.5 s), visual stimuli (flashing green light-emitting diode [LED], 0.5 s, to right eye), or touch stimuli (10 Hz vibrating piezoelectric actuator applied to left whiskers), to elicit responses in the

respective sensory cortices. All three modalities produced activity primarily in the expected sensory cortical areas, comparably in both Gad2<sup>+</sup> and VGlut1<sup>+</sup>, but not in GFP control mice, and specifically in the contralateral cortex for visual and touch stimuli (red arrowheads in Figures 3G–3I; quantification in Figure 3J). Activity was also observed to a lesser extent in regions that receive projections from primary sensory areas, in line with previous observations using voltage-sensitive dyes (Ferezou et al., 2007; Mohajerani et al., 2013). Furthermore, and also as expected, signals from excitatory and inhibitory neurons tracked each other during these passive responses to sensory stimuli (Figures 3G–3J).

Because wide-field microscopy cannot isolate signals from single cells, we next used two-photon microscopy to investigate the likely source of the wide-field whole-cortex activity dynamics. Using mice performing the olfactory go/no-go task, we registered videos recorded with the wide-field macroscope through a 7 mm cranial window with the calibration image used for registering fields of view acquired through two-photon imaging. By extracting the wide-field signal corresponding to each field of view acquired through two-photon imaging, we could directly compare the local fluorescence traces from each region recorded by the two imaging modalities (Figures 3K and 3L). In addition to the L2/3 data sets described in Figure 1, we recorded from layer 1 (L1) neuropil in several locations across the cortex (for  $n = 3$  VGlut1<sup>+</sup> mice,  $n = 21$  L1 regions,  $n = 62$  L2/3) (Figures 3K and 3L). We found that the summed full-frame L1 fluorescence was significantly more correlated with the corresponding wide-field signal than was full-frame L2/3 fluorescence (Figure 3M; average  $R = 0.45$  versus  $R = 0.12$ ,  $p < 0.01$ , Wilcoxon rank-sum test).

These data suggest that the widespread signals observed through wide-field imaging in excitatory neurons reflect primarily superficial neuropil activity, comprising axonal inputs and local dendritic dynamics. This L1 contribution to the wide-field signal is expected given that both blue excitation and green emission light will attenuate rapidly by scattering in mature brain tissue (Aravanis et al., 2007), and because the whole-cortex expression approach labels axons and dendrites in addition to somata. In VGlut1<sup>+</sup> L1 excitatory neuropil, the bulk  $\text{Ca}^{2+}$  signal likely represents both axonal and dendritic fluorescence. The axonal contribution to this signal includes recurrent cortico-cortical feedback connections that have been proposed to modulate activity in other cortical regions during goal-directed behavior (Cauller, 1995; Miller and Cohen, 2001) and that have previously been shown to encode different forms of task-related information during multiple behaviors (Makino and Komiya, 2015; Petreanu et al., 2012). In addition, this signal likely includes a large contribution from local L5 pyramidal cell dendrites, which can exhibit  $\text{Ca}^{2+}$  transients in response to synaptic input, back-propagating action potentials, or dendritic spiking (Stuart and Spruston, 2015). By contrast, inhibitory neurons in cortex are thought to be primarily local interneurons, meaning that Gad2<sup>+</sup> wide-field signals most likely represent local activity (Kepcs and Fishell, 2014). Measuring both these signals in superficial neuropil throughout cortex using wide-field microscopy is therefore important to test theories of the widespread broadcast of task-related information during goal-directed behavior.

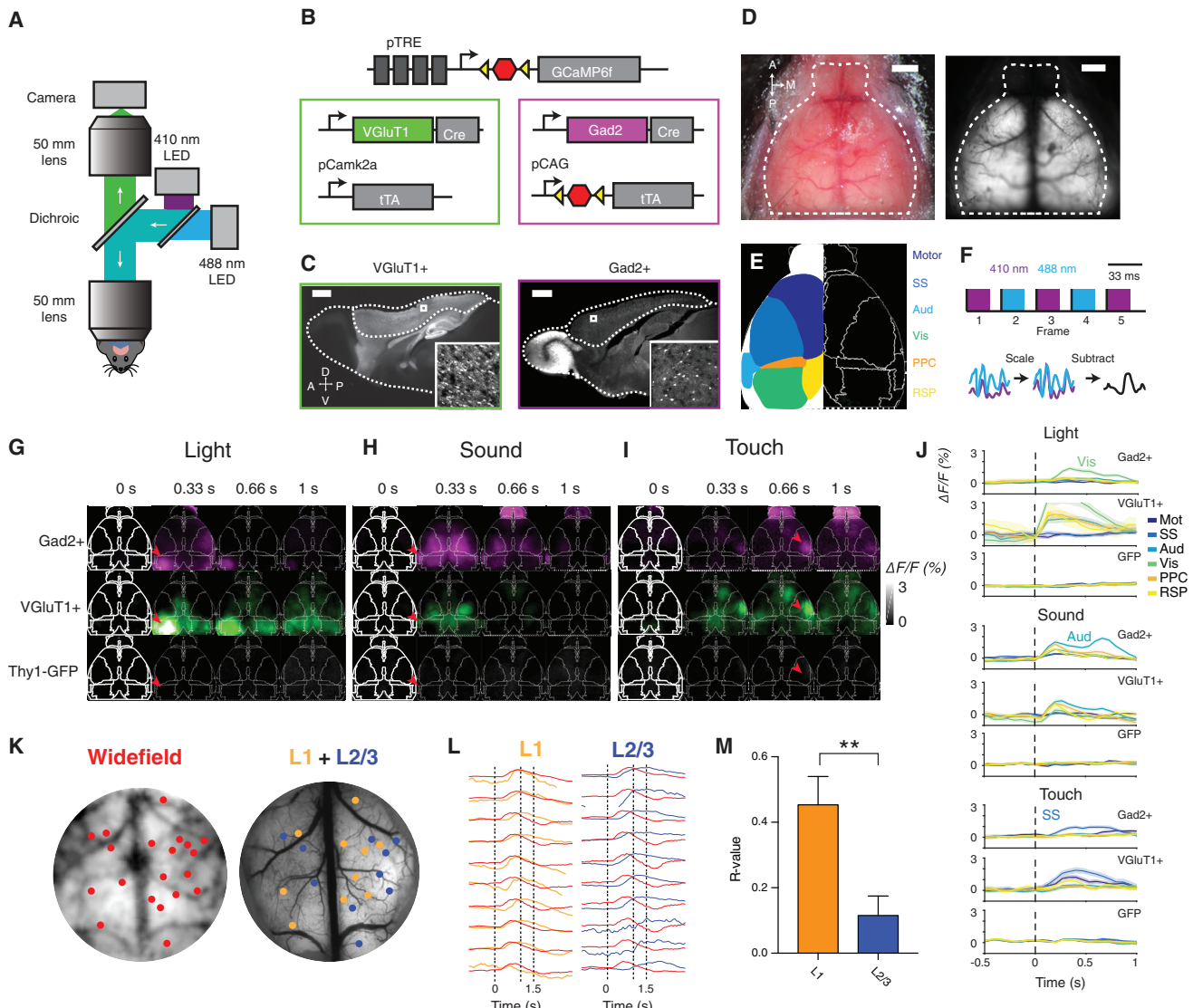


**Figure 3. Cell-Type-Specific Synchronous Cortex-wide Imaging of Neural Activity**

- (A) Macroscope schematic for whole-cortex wide-field imaging.
- (B) Diagram of genetic strategy for expression of GCaMP6f in all inhibitory or excitatory neurons.
- (C) GCaMP6f expression in VGlut1<sup>+</sup> and Gad2<sup>+</sup> brains, with cortex outlined. Inset: individual VGlut1<sup>+</sup> and Gad2<sup>+</sup> neurons expressing GCaMP6f.
- (D) Left: bright-field image of mouse skull with clear cap. Right: transcranial fluorescence of excitatory neurons.
- (E) Diagram of cortical regions overlaid on atlas.
- (F) Blood-volume autofluorescence subtraction process. Top: schematic of alternating illumination sequence. Bottom: schematic of per-pixel blood fluorescence normalization scheme.
- (G–I) Normalized fluorescence response of VGlut1<sup>+</sup>, Gad2<sup>+</sup>, and control mice to sensory stimuli, averaged across more than ten trials for a single mouse. Time points indicate end of integration window. (G) Flashing LED delivered to right eye for 0.5 s. Arrowhead indicates primary visual cortex. (H) Fifteen kilohertz auditory tone stimulation, delivered for 0.5 s. Arrowhead indicates primary auditory cortex. (I) Vibrating touch stimulus delivered to left whiskers for 0.5 s. Arrowhead indicates primary somatosensory cortex.
- (J) Regional time series corresponding to (G), (H), and (I) in a VGlut1<sup>+</sup>, Gad2<sup>+</sup>, and GFP mouse, averaged across 30 stimulus presentations. For each stimulus, the indicated corresponding primary sensory region has the largest response. Error bars, SEM.
- (K) Co-registration of average wide-field fluorescence and wide-field two-photon calibration image, allowing for the direct comparison of wide-field and two-photon signals from the same location in cortex. Orange dots indicate fields of view acquired at layer 1 (0–150 µm below the surface), and blue dots indicate fields of view acquired at layer 2/3 (150–350 µm below the surface).
- (L) Overlaid average, maximum-normalized traces from several representative regions acquired via wide-field (red) and the summed full-frame fluorescence from two-photon microscopy (neuropil + soma) in L1 and L2/3. Dashed lines indicate task events.
- (M) Average correlation between L1 and wide-field and between L2/3 and wide-field signals at equivalent locations. n = 21 L1 fields of view (FOVs), n = 62 L2/3 FOVs, from n = 3 mice. \*\*p < 0.01, Wilcoxon rank-sum test. Error bars, SEM.

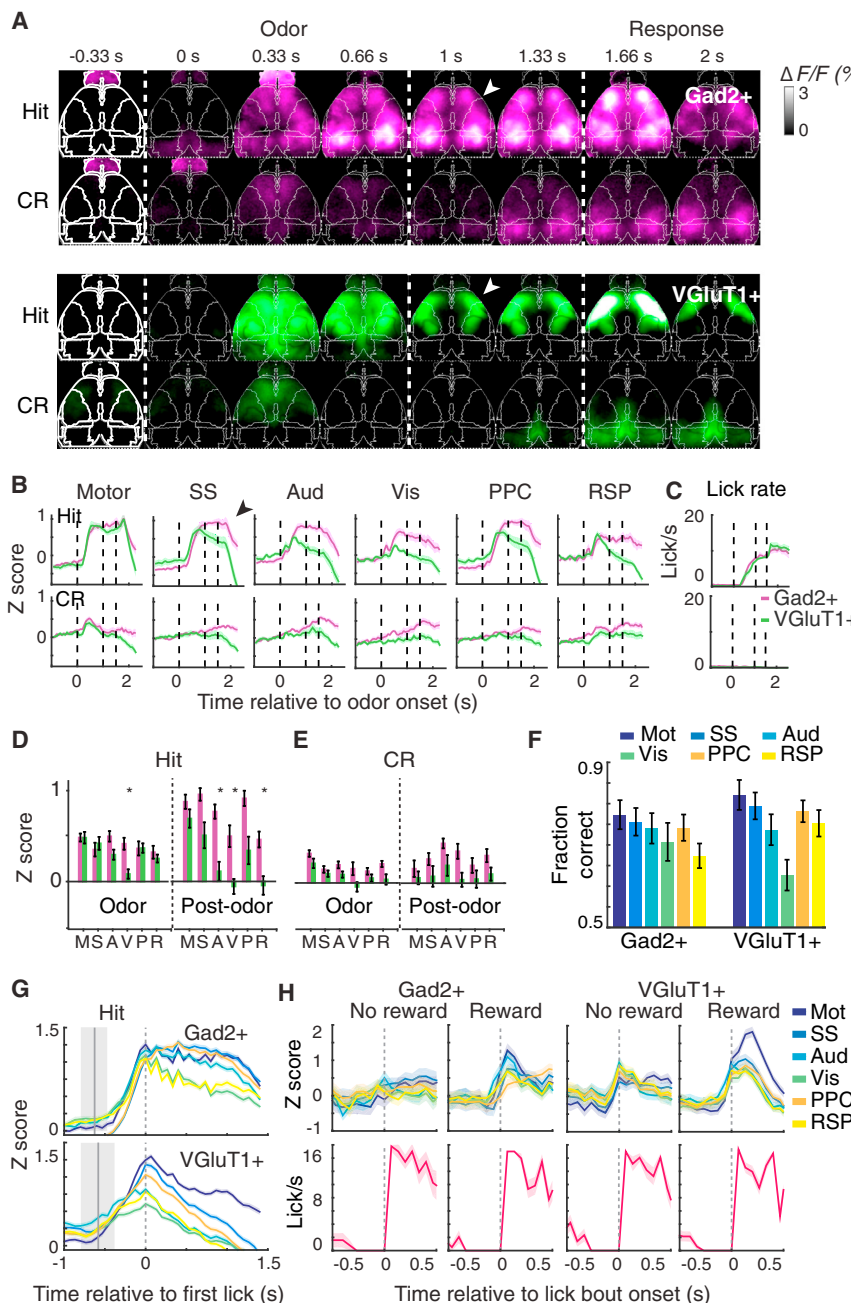


**Figure 4. Inhibitory and Excitatory Neural Dynamics Reflect Task Engagement**

(A) Example video sequence of average fluorescence across hit and correct reject (CR) trials in a Gad2<sup>+</sup> and VGlut1<sup>+</sup> mouse. White arrowheads indicate fronto-parietal bias of VGlut1<sup>+</sup> activity relative to the widespread Gad2<sup>+</sup> activation following odor cue period.

(B) Average traces from six cortical regions on hit and correct reject (CR), averaged across mice for 9 Gad2<sup>+</sup> and 12 VGlut1<sup>+</sup> mice. (Means of 62 hit and 53 CR trials per mouse for VGlut1<sup>+</sup> and 57 hit and 51 CR trials for Gad2<sup>+</sup>.) Error bars denote SEM. Black arrowhead indicates divergence between Gad2<sup>+</sup> and VGlut1<sup>+</sup> activity following the cue period in all regions except for motor cortex. (C) Average lick rate on hit and CR trials averaged across mice for 9 Gad2<sup>+</sup> and 12 VGlut1<sup>+</sup> mice. Error bars denote SEM.

(D) Average values from (B) during 1 s odor delivery period or 0.5 s post-odor period during Hit trial, across n = 9 Gad2<sup>+</sup> and 12 VGlut1<sup>+</sup> mice. \*p < 0.05, Wilcoxon rank-sum test, Bonferroni corrected.

(E) Same as (D), but for CR trial.

(F) ROC analysis of single-trial hit versus CR trial-type decoding across different cortical areas in Gad2<sup>+</sup> and VGlut1<sup>+</sup> mice.

(G) Timing of neural activity relative to behavioral onset in hit trials. The same data as in (B), aligned to the time of first lick and with different brain areas overlaid on the same scale. Gray region represents distribution of cue onset time relative to first lick.

(H) Un-cued task in which mice were rewarded only during a specific time window, while engaging in spontaneous bouts of licking. Top: overlaid traces of all seven cortical regions, aligned to beginning of lick bout, n = 2 Gad2<sup>+</sup> and 3 VGlut1<sup>+</sup>, with 32, 49, 19, and 29 pooled trials from left to right. Bottom: corresponding aligned lick rate.

All values in (F–H) and (J) are mean  $\pm$  SEM across mice and across pooled trials in (J). A, Aud, auditory; M, motor; p, PPC, posterior parietal; R, RSP, retrosplenial; S, SS, somatosensory; V, Vis, visual.

mean  $\pm$  SEM). Because the mice exhibited highly reliable behavior during the task (Figure 1C), we first analyzed the trial-averaged dynamics of activity across cortex in Gad2<sup>+</sup> and VGlut1<sup>+</sup> mice.

Both Gad2<sup>+</sup> and VGlut1<sup>+</sup> mice exhibited widespread synchronous cortical activation averaged across trials upon cue presentation during the task (Figures 4A and 4B), though with intriguing differences. In both cases, in hit trials, activity increased dramatically on average upon cue presentation and corresponding onset of anticipatory licking and stayed active until reward delivery, when the activity abruptly diminished despite the animal continuing to lick for several seconds (Figures 4B and 4C). Inhibitory Gad2<sup>+</sup> neuropil throughout neocortex was similarly active in both trial types during the cue period, whereas excitatory neuropil in the frontal motor and somatosensory cortex was

### Inhibitory and Excitatory Neural Dynamics Reflect Task Engagement

Next, to identify the globally broadcast task-related signals that could serve to coordinate cortical activity for a specific behavioral goal, we examined the pan-cortical activity patterns of inhibitory and excitatory neuropil using our transcranial imaging approach in mice performing the olfactory go/no-go task. Mice were imaged after passing a behavioral criterion of >70% trials correct per session (87%  $\pm$  7% correct across 9 Gad2<sup>+</sup> and 90%  $\pm$  9% correct across 12 VGlut1<sup>+</sup>, with 86%  $\pm$  1% and 87%  $\pm$  2% correct CR trials, respectively,

preferentially activated compared with posterior visual and retrosplenial cortex during the cue period (Figures 4B and 4C). The olfactory bulb also demonstrated interesting dynamics (Figure S3F), although because of the many differences between excitatory mitral/tufted cells and inhibitory granule cells of the olfactory bulb, and excitatory principal cells and inhibitory interneurons of the neocortex, a direct comparison with cortex is difficult. In all cortical areas and in both cell types, activity began to increase during the cue phase.

Surprisingly, between the cue and reward periods in both trial conditions, inhibitory neuropil continued to remain highly active, whereas the excitatory (VGluT1<sup>+</sup>) activity robustly decreased after the cue period (compare magenta and green traces across Figure 4B and summary statistics between the cue and reward periods in Figures 4D and 4E). These widespread patterns of activity were consistent across trials (example in Figures S3D and 3DE); ROC analysis showed that an ideal observer could distinguish between trial types (hit versus CR) >75% of the time on average by examining the activity on single trials in the majority of cortical regions, in both Gad2<sup>+</sup> and VGluT1<sup>+</sup> mice (Figure 4F). Alignment to the onset of licking revealed that in both types of mice, activity throughout cortex began ramping up several hundred milliseconds before the first recorded lick (Figure 4G), while control Thy1-GFP mice exhibited no mean activity changes throughout cortex during this task or on single trials (trial-averaged representative video in Figure S3A; single trials for representative mouse in Figure S3B; average traces across n = 3 mice in Figure S3C).

We confirmed this surprising finding of separable excitatory- and inhibitory-neuropil activity dynamics during behavior by using new methods for labeling both cell types within the very same animal for a simultaneous two-color imaging approach (Figures S5A–S5C). To increase the flexibility of wide-field imaging for incorporating advances in activity sensors, and to remove the need to breed additional triple-transgenic animals, we implemented a viral technique for brain-wide expression of GCaMP in specific cell types in adult animals. In Gad2-Cre mice, we used intravenous administration of AAV-PHP.B, a capsid variant engineered to efficiently cross the blood-brain barrier (Deverman et al., 2016), to simultaneously express jRCaMP1b in primarily excitatory cells under control of the CaMKIIα promoter, and Cre-dependent GCaMP6f in inhibitory cells under control of the ubiquitous EF1α promoter (Figures S4B–S4D).

The jRCaMP1b and GCaMP6f expressing cells were largely non-overlapping, although a small amount of co-labeling was observed ( $10\% \pm 1\%$ , across n = 3 mice in three fields of view per mouse, mean  $\pm$  SEM), consistent with previous reports using the CaMKIIα promoter in AAV9 (Cook-Snyder et al., 2015) (Figures S4D and S4E). Using a large cortical window to access the cortex, we confirmed the earlier finding shown here, although with lower signal-to-noise, particularly in the RCaMP signal. We found that activity dynamics in the two cell types were instantaneously correlated throughout cortex but that in a number of regions including visual, somatosensory, and posterior parietal, but not motor cortex, inhibitory neural activity persisted longer than excitatory activity in accordance with Figure 4 (Figures S4F–S4H, orange arrows in Figure S4G and black arrows in Figure S4H).

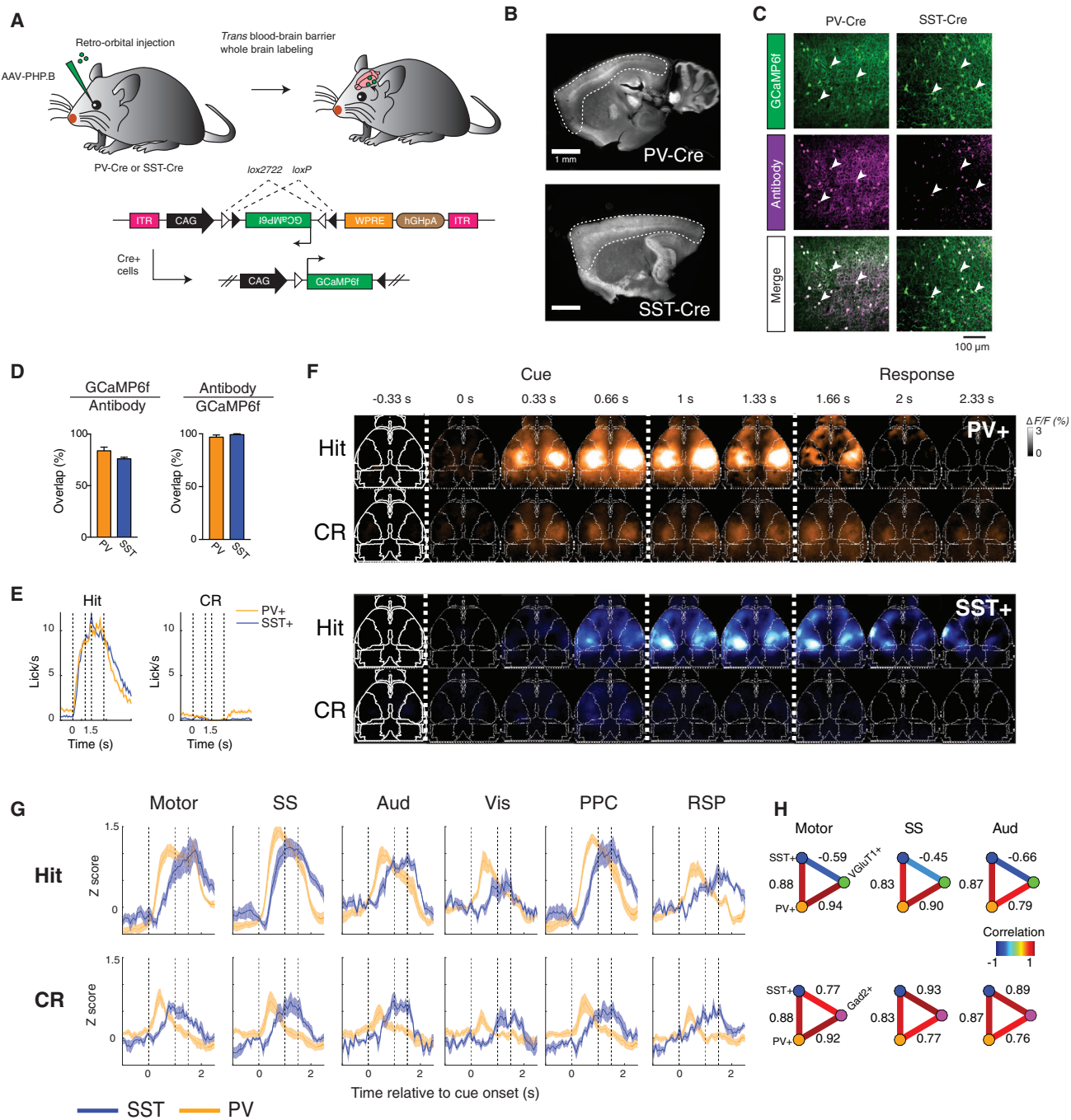
The abrupt shutoff of neuropil activity upon reward delivery despite a continuation of the licking behavior corroborated the earlier finding (see Figures 2E–2H) that these neural signals are not merely a byproduct of sensorimotor feedback during licking behavior. Nor are these signals simply a product of ongoing motor output (Figures 4B–4D), of reward receipt itself (Figures S5A, S5C, and S5D), or of unanticipated stimuli (Figures 3G–3J). Instead, these signals appear to represent the behavioral decision with anticipation of subsequent reward.

To further test that this widespread activation during hit trials was the consequence of an internal state related to the rewarded nature of the task, and not simply a consequence of the motor output (licking), we imaged a subset of the cohort during a different task, before training on the olfactory discrimination task. Here, mice (n = 2 Gad2<sup>+</sup>, n = 3 VGluT1<sup>+</sup>) were presented with a lick port, but no cues (olfactory, visual, or otherwise) were presented to indicate when water would be dispensed. Instead, mice could lick freely but were rewarded only within a certain time window (leading to reward on about 50% of the lick bouts). As seen in Figure 4H, mice licked at the same rate on rewarded and non-rewarded bouts, but only the rewarded case yielded full widespread neural activation, particularly in inhibitory neuropil. (In contrast, only a small increase in activity restricted to frontal cortex was attributable to reward delivery itself; quantified during the go/no-go task in both inhibitory and excitatory neurons; Figures S5A and S5C.) In particular, when summing across all regions, just 38% of the VGluT1<sup>+</sup> response and 31% of the Gad2<sup>+</sup> response could be explained by licking alone in the absence of reward (where percentage response is the ratio of the integral under the curve from time 0–0.3 s in the absence of reward to the integral of the curve in the presence of reward). This difference revealed that the conjunction of licking behavior in the setting of immediate or anticipated reward, but not licking in itself, produced the observed globally distributed neuropil activity dynamics.

### Cell-Type-Specific Interneuron Activity Dynamics

Although this initial level of discrimination between excitatory and inhibitory neuropil was informative, Gad2-expressing interneurons can be subdivided further into even more specific, molecularly defined classes that may play distinct roles in representing task-related information (Kepecs and Fishell, 2014; Pinto and Dan, 2015). Therefore, we next characterized the responses of two different interneuron populations during the same goal-directed task: perisomatic-targeting parvalbumin-expressing (PV<sup>+</sup>) and dendrite-targeting somatostatin-expressing (SST<sup>+</sup>) cell types, which respectively account for approximately 40% and 30% of all GABAergic interneurons in neocortex (Rudy et al., 2011). These two types of interneurons exhibit highly distinct and specific patterns of morphology, connectivity, and neuromodulator receptor expression and are thought to play distinct roles in circuit function (Kepecs and Fishell, 2014).

We produced additional recombinant AAV using the blood-brain barrier-crossing capsid variant AAV-PHP.B, carrying a Cre-dependent GCaMP6f gene driven by the strong CAG promoter to provide high enough expression for transcranial imaging (Deverman et al., 2016) (Figure 5A). Intravenously injected AAV-PHP.B into SST-Cre or PV-Cre mice produced expression

**Figure 5. Cell-Type-Specific Activity Dynamics in PV<sup>+</sup> and SST<sup>+</sup> Interneurons**

- (A) Diagram of strategy for whole-brain expression of GCaMP6f in all SST<sup>+</sup> or PV<sup>+</sup> interneurons via systemic viral infection.
- (B) Wide-field image of GCaMP6f expression in SST-Cre and PV-Cre brains, with cortex outlined (stained with anti-GFP).
- (C) GCaMP6f expression (stained with anti-GFP) in a PV-Cre or SST-Cre mouse, and co-staining with PV or SST antibody. White arrowheads indicate cells co-expressing GCaMP6f and PV or SST.
- (D) Overlap between GCaMP and PV or SST staining to quantify the efficiency (GCaMP6f/antibody) and specificity (antibody/GCaMP6f) of viral targeting, from  $n = 3$  mice per condition and three fields of view per mouse. Mean  $\pm$  SEM.
- (E) Average licking behavior on hit and CR trials across  $n = 5$  SST-Cre and  $n = 7$  PV-Cre mice performing the olfactory go/no-go task, mean  $\pm$  SEM.
- (F) Example video sequence of average fluorescence across hit and correct reject (CR) trials, in a representative PV-Cre and SST-Cre mouse.
- (G) Average traces from six cortical regions on hit and correct reject (CR) trials, averaged across mice for  $n = 5$  SST-Cre and 7 PV-Cre mice. Error bars, SEM.

(legend continued on next page)

of GCaMP in each cell type across the entire cortex (Figure 5B), at a level sufficient for intact-skull wide-field imaging. Immunostaining for GFP and either parvalbumin or somatostatin revealed high-efficiency labeling ( $83\% \pm 3.5\%$  for PV and  $76\% \pm 1.5\%$  for SST) of the correct cell type, with little leak expression ( $97\% \pm 2\%$  for PV and  $99\% \pm 1\%$  for SST coexpress PV or SST out of all GCaMP+,  $n = 3$  fields of view per mouse across  $n = 3$  mice, mean  $\pm$  SEM) (Figures 5C and 5D).

Mice ( $n = 6$  PV<sup>+</sup>,  $n = 4$  SST<sup>+</sup>) were imaged while performing the olfactory go/no-go decision-making task. Mice of the two genotypes exhibited the same average licking response to the odor cue (Figure 5E). The spatial pattern of activation in both cell types was qualitatively similar to that observed in Gad2<sup>+</sup> mice (Figure 5F), with both types of cells exhibiting task-related activation throughout dorsal cortex. However, we found that the PV<sup>+</sup> and SST<sup>+</sup> interneurons displayed a striking temporal offset in their activity dynamics (Figures 5F and 5G). Whereas the activity of PV<sup>+</sup> neuropil peaked during the cue period and then began to decay (similar to the VGlut1<sup>+</sup> neurons; Figures 5F and 5G), SST<sup>+</sup> neuropil activity peaked after a relative delay and then sustained a plateau level of activity before decay. PV<sup>+</sup> neuropil exhibited widespread transient activity immediately following cue onset on CR trials, whereas SST<sup>+</sup> neuropil became active during the cue several hundred milliseconds later (Figures 5F and 5G).

To quantify this difference in activity dynamics, we compared the correlation of PV<sup>+</sup> and SST<sup>+</sup> traces to the VGlut1<sup>+</sup> and Gad2<sup>+</sup> traces (Figure 5H). Using the Pearson linear correlation coefficient, the PV<sup>+</sup> and SST<sup>+</sup> average traces (across mice) were positively correlated with each other across all brain regions, as both types of neurons increase their activity in relation to the cue ( $p < 5 \times 10^{-5}$ , two-tailed test from bootstrap confidence interval; STAR Methods). Because of this shared correlation, we used the linear partial correlation coefficient to then compare PV<sup>+</sup> with Gad2<sup>+</sup> and VGlut1<sup>+</sup>, while taking into account and controlling for the correlation shared with SST<sup>+</sup> (and vice versa). Whereas Gad2<sup>+</sup> activity was positively correlated across all regions with that of both PV<sup>+</sup> and SST<sup>+</sup> as expected, VGlut1<sup>+</sup> was positively partially correlated with PV<sup>+</sup> but negatively partially correlated with SST<sup>+</sup> ( $p < 5 \times 10^{-5}$ , two-tailed test from bootstrap confidence interval). Transcranial wide-field imaging thus revealed the surprising result that a single behaviorally induced global brain state can involve separable global dynamics of different molecularly defined cell types in the same cortical area.

### Premotor Cortex Activity Is Necessary and Sufficient for Widespread Cortical Activation

Because goal-directed licking during the go/no-go task correlated with recruitment both of single cells throughout cortex and of widespread activity in inhibitory and excitatory neuropil, we next sought to test the causal relationship between the initiation of licking behavior and globally coordinated cortical activity. Using VGAT-ChR2 transgenic mice, we first performed a coarse survey to find cortical regions necessary for performance

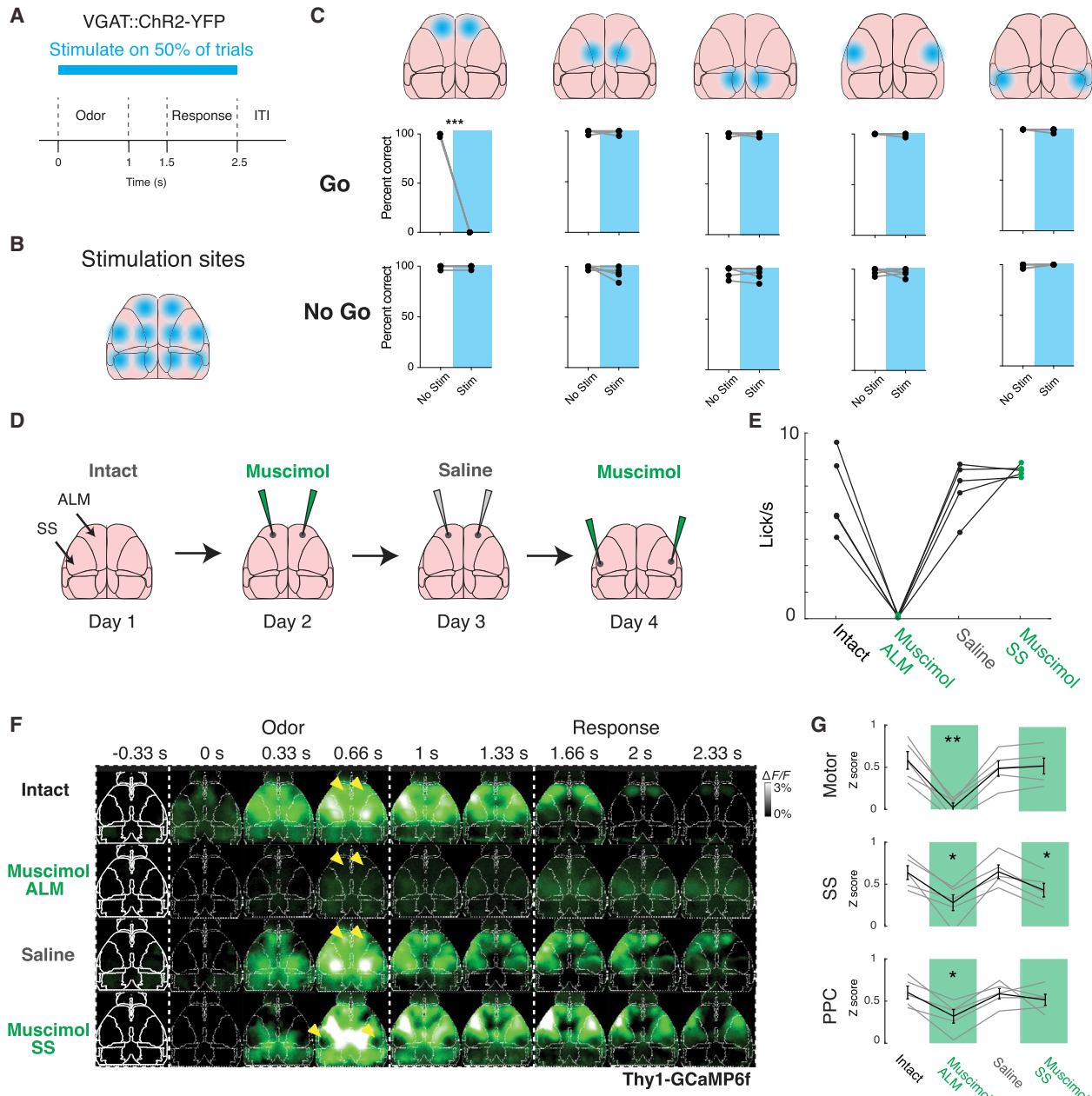
of the go/no-go task (Goad et al., 2016; Guo et al., 2014). In well-trained mice, we systematically bilaterally inhibited five different cortical regions by optogenetically activating GABAergic interneurons within an ~2 mm diameter disk during the cue through reward period of the task, on a randomly selected set of trials within a session (Figures 6A and 6B). We found that among the regions probed, only inhibiting the frontal cortical region prevented licking for water on go trials (Figure 6C;  $p < 0.001$ , paired t test,  $n = 5$  mice, 100 total trials per region). On trials without illumination, all mice performed normally, and the inhibition had no effect on performance on no-go trials in any area tested.

The frontal region of inhibition contains the anterior-lateral premotor cortex (ALM), which has been previously implicated in initiating voluntary lick behavior: electrical stimulation of ALM produces lick motions, and inhibition of ALM with muscimol, an agonist of GABA<sub>A</sub> receptors, or optogenetic activation of inhibitory interneurons specifically inhibits voluntary licking without affecting other behaviors (Guo et al., 2014; Komiyama et al., 2010). ALM has been shown to exhibit more complex representations such as short-term memory during motor planning (Goad et al., 2016; Li et al., 2015). Furthermore, in addition to its output to tongue motor nuclei in the brainstem, ALM projects broadly to other parts of the cortical somatomotor system (Zingg et al., 2014), and is thus positioned as a potential hub for broadcasting task-related information to other parts of cortex. Despite these behavioral and anatomical results, the effects of ALM inhibition on global cortical activity during behavior remain unknown.

Therefore, to test the relationship between goal-directed behavior and brain-wide activity, we used ALM pharmacological inhibition to specifically prevent the mouse from engaging in voluntary licking while still being able to sense the stimulus and otherwise behave normally. This experimental design (Figure 6A) enabled comparison of whole-cortex activity during ALM inhibition with several control conditions. First, clear-skull prepared mice ( $n = 5$ ) were trained to a near perfect level of performance; next, mice were imaged while performing the olfactory go/no-go task on four consecutive days, after one of (1) no injection, (2) bilateral injection of muscimol into ALM, (3) control bilateral injection of saline into ALM, or (4) a control bilateral injection of muscimol into barrel cortex. Because of the limited number of VGlut1<sup>+</sup> triple transgenic mice, we used Thy1-GCaMP6f mice, which express GCaMP6f in a large subset of (primarily) excitatory cortical neurons (Dana et al., 2014).

In concordance with our optogenetic results, silencing ALM with muscimol successfully inhibited voluntary licking; behavior was otherwise normal, and mice recovered the ability to lick by the subsequent day. In contrast, silencing barrel cortex with muscimol had no impact on behavioral performance (Figure 6B). In comparison with the baseline day (Figure 6C, top row), injecting muscimol into ALM effectively blocked widespread cortical activation in response to the cue (Figure 6C, second row). The region corresponding to the injection site was completely silent (yellow arrows) as expected, while the rest of

(H) Partial correlations between PV<sup>+</sup>, SST<sup>+</sup> and VGlut1<sup>+</sup> or Gad2<sup>+</sup> signals to show cell-type-specific correlations to inhibitory or excitatory activity. Positive correlation between PV<sup>+</sup> and SST<sup>+</sup> average traces in all brain regions (Pearson linear correlation coefficient,  $p < 5 \times 10^{-5}$ ); linear partial correlation between PV<sup>+</sup> and VGlut1<sup>+</sup> or Gad2<sup>+</sup> while controlling for the correlation shared with SST<sup>+</sup>, and between SST<sup>+</sup> and VGlut1<sup>+</sup> or Gad2<sup>+</sup> while controlling for correlation shared with PV<sup>+</sup> ( $p < 5 \times 10^{-5}$  across all brain regions, positive for PV<sup>+</sup>: VGlut1<sup>+</sup>, PV<sup>+</sup>: Gad2<sup>+</sup>, and SST<sup>+</sup>: Gad2<sup>+</sup>, and negative for SST<sup>+</sup>: VGlut1<sup>+</sup>).

**Figure 6. Premotor Cortex Activity Is Necessary for Widespread Cortical Activation**

(A) Diagram of paradigm of cortical inhibition using VGAT::ChR2-YFP stimulation through a clear skull cap. Mice were stimulated randomly on 50% of trials during the odor through response epochs of the task.

(B) Diagram of bilateral sites for cortical inhibition tiling the skull.

(C) Results of bilateral optogenetic inhibition in five regions tiling the skulls of  $n = 5$  VGAT::ChR2-YFP mice, separately on go and no-go trials. Correct go trials, hit; correct no-go, correct reject. \*\*\* $p < 0.001$ , paired t test, Benjamini-Hochberg corrected.

(D) Diagram of ALM (premotor lick cortex) silencing experiment to determine its role in the production of global cortical activity. Well-trained Thy1-GCaMP6f mice are imaged while performing the olfactory go/no-go task on subsequent days with no injection, bilateral injection of muscimol into ALM, bilateral injection of saline into ALM, and bilateral injection of muscimol into somatosensory (barrel) cortex.

(E) Average licking behavior on go trials (during 1 s after cue) in intact mice and after muscimol injection into ALM, saline injection into ALM, and muscimol injection into barrel cortex. Each dot per day represents an animal ( $n = 5$ ).

(F) Example video sequences of average fluorescence during go trials after each injection. Arrowheads in first three rows indicate ALM; arrowhead in last row indicates barrel cortex.

(G) Average Z-scored fluorescence during 2 s spanning odor through response period in three cortical regions. Mean  $\pm$  SEM in black, individual mice in gray, across  $n = 5$  mice. \*\* $p < 0.01$ , \* $p < 0.05$ , one-sided paired t test with baseline day, Benjamini-Hochberg corrected.

the cortex exhibited significantly decreased activation (quantified in Figure 6D for motor, somatosensory, and parietal cortices;  $p < 0.05$  for somatosensory and parietal,  $p < 0.01$  for motor, one-sided paired t test with intact condition, Benjamini-Hochberg correction). In contrast, after similar silencing of barrel cortex (Figure 6D, fourth row, yellow arrows), other cortical regions maintained largely indistinguishable levels of activation. Together these data supported the hypothesis that ALM-mediated initiation of goal-directed licking behavior is necessary for the elicitation of cortex-wide activity in superficial neuropil.

Although this silencing experiment revealed the necessity of ALM for producing widespread task-related signals in cortex, we sought to determine whether ALM activation alone in naive mice was sufficient to produce this activity even in the absence of a task. To this end, we simultaneously optogenetically activated excitatory neurons in ALM of naive mice while imaging the rest of cortex (Figures S6A and S6B). We used a red-shifted excitatory opsin (Klapoetke et al., 2014) driven by the CaMKII $\alpha$  promoter and carried by AAV injected bilaterally into ALM to activate excitatory neurons in clear-skull prepared Thy1-GCaMP6f mice (Figures S6A and S6B). Bilateral optogenetic stimulation using 594 nm illumination at 10 Hz reliably produced licking behavior, whereas control mice injected with AAV containing CaMKII $\alpha$ ::mCherry showed neither licking response nor cortical activation upon stimulation (Figures S6C and S6D). Simultaneous wide-field recording showed that optogenetic stimulation produced activity spanning the majority of cortex, with statistically significant activation in motor, somatosensory, and parietal cortices (Figures S6E, S6F, and S6I). By contrast, CaMKII $\alpha$ ::mCherry injected mice showed no consistent activation in any area (Figures S6G, S6H, and S6J). Activity in ALM excitatory neurons is therefore sufficient both to produce licking behavior and cause widespread cortical activity.

## DISCUSSION

Here we find that goal-directed behavior produces broadly distributed task-related activity throughout the neocortex, reflected both in widespread single cell and in neuropil activity. Different molecularly defined cell types contribute specific activity patterns to this global state. We further demonstrate that a single premotor cortical region responsible for the production of goal-directed licking behavior is necessary for these global cortical dynamics in response to task cues. Together, these observations provide a new kind of experimental support for the concept that widely broadcast task-related information could serve to coordinate cortical activity for a single, unitary behavioral goal.

A variety of previous indirect lines of evidence are consistent with this concept of widespread representations of task information. Human fMRI studies show that a distinct “task-positive” cortical network is active during a variety of cognitive tasks (Fox et al., 2005), and electroencephalographic (EEG) studies have revealed large-scale patterns of coherence during performance of go/no-go tasks (Shibata et al., 1997). Different regions of cortex, including prefrontal cortex and primary sensory areas, exhibit dynamically modulated synchrony as a function of attention, anticipation, or expectation during behavior (Bressler et al.,

1993; Gilbert and Li, 2013; Ledberg et al., 2007; Miller and Buschman, 2013). Many local neurophysiological studies during behavior have revealed task-dependent patterns of neural activity in cortex that do not correlate with specific sensory or motor variables but that seem to represent internal state variables such as task engagement, attention, or expectations (Kobak et al., 2016; Poort et al., 2015). Indeed, a few studies comparing the activity of single cells or local field potentials in different cortical regions in non-human primates and mice performing perceptual decision-making tasks have shown that task-relevant variables, including behavioral decisions, are encoded in more than one location, albeit in cortical regions expected a priori to be involved in the behavior (Goad et al., 2016; Hernández et al., 2010; Ledberg et al., 2007; Siegel et al., 2015). These results hint that cortical activity could similarly reflect global task-related states at the single-cell level. Yet little work prior to this study has systematically explored the neuronal or circuit basis of these signals, despite their potential importance in cortical function.

We discovered that activity throughout the cortex in single cells, cell types, and superficial neuropil, signal distinct aspects of task-related information. The activity in all cell types was tied to task events and partially decoupled from the animal’s behavior, suggesting that it represented task information rather than simply sensorimotor feedback from ongoing behavior. Single cells tended to encode task timing more reliably than trial-by-trial variation in motor action (Figures 2E and 2F) and were primarily active during the period from cue to reward (Figures 1G and 1H). These cells were distributed in a salt-and-pepper manner throughout the observable part of the cortex (Figures 1I, 2A, 2E, and 2H), distinct from highly specific regional coding of sensory information (Ohki et al., 2005). Similarly, the wide-field activity in both inhibitory and excitatory neurons was limited to spanning the duration of the task from the cue to the reward, despite the licking behavior continuing beyond the reward delivery for several seconds (Figures 4B and 4C), and unrewarded spontaneous behavior did not produce equivalent widespread activation (Figure 4H).

Resolving these wide-field signals by cell type revealed distinguishable underlying neural dynamical processes. The L1 signal of VGlut1 $^+$  mice is composed of both axonal and dendritic signals. For the axonal contribution, the transmission of “top-down” internal state signals through long-range excitatory feedback axon projections would be ideally suited to globally coordinate cortical activity to specific ends by biasing the inputs to local neuronal populations (Cauller, 1995; Makino and Komiya, 2015; Petreanu et al., 2012). The dendritic component of VGlut1 $^+$  neuropil signal likely reflects the integration of these and other inputs in the dendrites of local L5 pyramidal neurons (Stuart and Spruston, 2015). Further investigation of L5 somatic activity will be required to determine whether and how these widespread inputs are transformed into local spiking output of L5 pyramidal neurons, in addition to the widespread somatic activity we observed in L2/3 through two-photon Ca $^{2+}$  imaging (Figure 1). By contrast, because cortical GABAergic neurons are primarily local interneurons (Kepcs and Fishell, 2014), the widespread signals we observed from inhibitory Gad2 $^+$  neurons (including PV $^+$  and SST $^+$ ) most likely reflect local interneuron activity.

To perform these measurements in these specific interneuron cell types, we implemented a new viral-genetic approach for expressing fluorescent  $\text{Ca}^{2+}$  sensors throughout the brain. This approach revealed differences in the timing of activity between  $\text{PV}^+$  and  $\text{SST}^+$  inhibitory interneurons, with perisomatic-targeting  $\text{PV}^+$  neuron activity preceding dendrite-targeting  $\text{SST}^+$  activity. These different types of interneurons have been described in many recent studies as playing distinct roles in cortical computation (Kvitsiani et al., 2013).  $\text{PV}^+$  neurons are thought to receive dense, nonspecific local input from nearby principal neurons (Harris and Mrsic-Flogel, 2013; Pfeffer et al., 2013), explaining their tight correlation with the  $\text{VGlut1}^+$  activity (Figure 5G), whereas  $\text{SST}^+$  neurons are known to locally inhibit  $\text{PV}^+$  neurons in visual cortex (Pfeffer et al., 2013), exhibit specific forms of experience-dependent plasticity (Makino and Komiyama, 2015), and have been shown to play a key role in integrating input from L1 excitatory feedback projections in visual cortex (Zhang et al., 2014). The offset between  $\text{PV}^+$  and  $\text{SST}^+$  neuron activity may represent a form of temporal gating, where first local excitatory populations are recruited by long-range excitatory projections, causing a fast compensatory response in  $\text{PV}^+$  neurons before slower  $\text{SST}^+$ -neuron mediated dendritic inhibition blocks further L1 inputs.

A variety of mechanisms—direct cortico-cortical connections, indirect cortico-thalamic-cortical connections, or common inputs from neuromodulators or other broadly projecting systems—could contribute to the observed widespread correlated activity between disparate regions of cortex. At the level of spatial resolution of our optogenetic inhibition, frontal cortex, including ALM, was the only area necessary for the performance of the task (Figure 6) and was necessary on an individual trial-by-trial basis. Our further result that pharmacological inhibition of the same area was necessary for both the voluntary licking behavior and cortex-wide neuropil response (Figure 6), however, implicates ALM as a potential hub or source of such global coordination. By contrast, although many other cortical regions also exhibited task-related activity, optogenetic inhibition in those regions had no effect on behavior. In particular, somatosensory cortex exhibited high levels of task-related activity yet muscimol inhibition in that region had no effect on behavior or on global cortical activation. Task-related activity observed in a particular region during behavior thus may represent broadly distributed signals informing local populations about the overall behavioral state in order to coordinate activity, beyond the more typical interpretation of task-related activity representing specific local roles of that region of the brain. Consistent with this concept, it was recently shown in nonhuman primates that an extensively studied cortical area carrying task-related signals during a motion discrimination task may be actually unnecessary for task performance (Katz et al., 2016).

These widespread coordinated patterns of activity in single cells may be a general feature of nervous system function, because comprehensive recording of activity from the majority of neurons (in animals in which this is possible, such as larval zebrafish and *Caenorhabditis elegans*) reveal global dynamical patterns that appear to encode behavioral states (Ahrens et al., 2013; Kato et al., 2015). New large field-of-view two-photon microscopes allow for single-cell measurements of activity within

multiple cortical regions simultaneously, but so far this approach can only sample activity throughout the whole cortex at low frame rates ( $\sim 1$  Hz) and non-synchronously (Sofroniew et al., 2014; Stirman et al., 2016). Two-area correlations in cortex have recently been reported using dual-area two-photon microscopes during goal-directed behavior; for example, Chen et al. (2016) reported that goal-directed behavior increased local coordination of activity within somatosensory cortex (between primary and secondary).

Future studies will also further advance our specific, mechanistic understanding of the means by which the widespread task-related information we observe can coordinate activity throughout cortex. One approach may be to compare pan-cortical activity across a variety of behaviors, involving different sensory modalities, actions, and expectations, ideally within the same animal, in order to determine how cortical activity is flexibly remapped for different goals. Understanding these mechanisms may be important clinically, as disrupted or abnormal communication between cortical regions has been widely proposed to play a crucial role in psychiatric disorders such as schizophrenia (Spellman and Gordon, 2015). Identification of failures in cortical communication using the methodologies developed for this study during disease-related states (Rajasethupathy et al., 2016) may in the long run point to future minimally invasive interventions to treat these disorders in human beings.

## STAR★METHODS

Detailed methods are provided in the online version of this paper and include the following:

- **KEY RESOURCES TABLE**
- **CONTACT FOR REAGENT AND RESOURCE SHARING**
- **EXPERIMENTAL MODEL AND SUBJECT DETAILS**
- **METHOD DETAILS**
  - Animal behavior
  - Two-photon imaging
  - Widefield imaging
  - Local inactivation experiments
  - Widefield Imaging (detailed description)
  - Stimulus Delivery
  - Widefield Image Registration
  - Olfactory Behavioral Setup
  - Histology and Immunohistochemistry
  - AAV-PHP.B Production and Intravenous Administration
  - Optogenetic Inactivation Experiments
  - Muscimol Inactivation Experiments
  - Optogenetic Activation
  - Two-photon Imaging
- **QUANTIFICATION AND STATISTICAL ANALYSIS**
  - Statistical analysis
  - Widefield analysis
  - Two-photon analysis
  - Clustering Analysis
  - ROC Analysis
  - Model-based Analysis

**SUPPLEMENTAL INFORMATION**

Supplemental Information includes six figures and one movie and can be found with this article online at <http://dx.doi.org/10.1016/j.neuron.2017.04.017>.

**AUTHOR CONTRIBUTIONS**

W.E.A., I.V.K., and K.D. designed the project and the experiments, with much input from L.L. on experimental setup, mouse genetics, and olfactory behavior. W.E.A. and I.V.K. performed the wide-field and two-photon imaging experiments, wrote the data acquisition software, and performed the analysis. I.V.K. and W.E.A. designed, and I.V.K. built, the macroscope and fluorescence normalization system. W.E.A. performed the histological analysis, with assistance from M.Z.C. I.V.K. built the two-color wide-field imaging setup. W.E.A. performed the muscimol experiment. I.V.K. and W.E.A. performed the optogenetic stimulation experiments, and I.V.K. built the optogenetic stimulation apparatus and software. W.E.A. built the olfactory behavioral apparatus; bred, genotyped, and trained the mice; and performed the surgeries, with assistance from M.Z.C. E.B.R. and W.E.A. implemented the GLM model for two-photon data analysis, and S.J.Y. assisted with software for two-photon image processing. K.C., V.G., and B.E.D. contributed AAV-PHP.B virus. W.E.A., I.V.K., and K.D. wrote the paper with input from L.L. K.D. supervised all aspects of the work.

**ACKNOWLEDGMENTS**

We would like to thank C. Ramakrishnan for molecular biology assistance and for cloning the CAG-DIO-GCaMP6f construct, J. Fernandez-Alcudia (Stanford Gene Vector and Virus Core) for producing AAV-PHP.B, H. Zeng (Allen Institute for Brain Science) for providing transgenic mice prior to publication, J. Sanders (Cold Spring Harbor Laboratory) for providing Bpod code and hardware designs, T. Komiyama (University of California, San Diego) for providing initial olfactometer advice, N. Young for image acquisition code, Z. Guo and K. Svoboda (Janelia Research Campus) for advice on the surgical preparation, and C. Manalac for assistance with genotyping. We are grateful to members of the K.D. and L.L. laboratories for comments and advice, particularly M. Lovett-Barron, P. Rajasethupathy, C. Kim, and A. Andelman. V.G. is a Heritage Principal Investigator supported by the Heritage Medical Research Institute. AAV-PHP.B work was funded by NIH grant DP2/PECASE (V.G.) and by the Beckman Institute at Caltech (V.G. and B.E.D.) through the Resource Center on CLARITY, Optogenetics, and Vector Engineering. K.D. and L.L. are Investigators of the Howard Hughes Medical Institute and are supported by a Hughes Collaborative Innovation Award. W.E.A. and I.V.K. were supported by National Science Foundation Graduate Research Fellowships (grant DGE-114747) and W.E.A. by a Fannie & John Hertz Foundation Fellowship. K.D. is supported by the Defense Advanced Research Projects Agency Neuro-FAST program, the National Institute of Mental Health, the National Institute on Drug Abuse, the National Science Foundation, the NOMIS Foundation, the Tarlton Foundation, the Wiegers Family Fund, the Nancy and James Grosfeld Foundation, the H.L. Snyder Medical Foundation, and the Samuel and Betsy Reeves Fund. All tools and methods are distributed and supported freely.

Received: June 17, 2016

Revised: January 26, 2017

Accepted: April 11, 2017

Published: May 17, 2017

**REFERENCES**

- Ahrens, M.B., Orger, M.B., Robson, D.N., Li, J.M., and Keller, P.J. (2013). Whole-brain functional imaging at cellular resolution using light-sheet microscopy. *Nat. Methods* 10, 413–420.
- Akemann, W., Mutoh, H., Perron, A., Park, Y.K., Iwamoto, Y., and Knöpfel, T. (2012). Imaging neural circuit dynamics with a voltage-sensitive fluorescent protein. *J. Neurophysiol.* 108, 2323–2337.
- Aravanis, A.M., Wang, L.P., Zhang, F., Meltzer, L.A., Mogri, M.Z., Schneider, M.B., and Deisseroth, K. (2007). An optical neural interface: in vivo control of rodent motor cortex with integrated fiberoptic and optogenetic technology. *J. Neural Eng.* 4, S143–S156.
- Bressler, S.L., Coppola, R., and Nakamura, R. (1993). Episodic multiregional cortical coherence at multiple frequencies during visual task performance. *Nature* 366, 153–156.
- Buschman, T.J., and Miller, E.K. (2007). Top-down versus bottom-up control of attention in the prefrontal and posterior parietal cortices. *Science* 315, 1860–1862.
- Caulier, L. (1995). Layer I of primary sensory neocortex: where top-down converges upon bottom-up. *Behav. Brain Res.* 71, 163–170.
- Chen, J.L., Carta, S., Soldado-Magraner, J., Schneider, B.L., and Helmchen, F. (2013a). Behaviour-dependent recruitment of long-range projection neurons in somatosensory cortex. *Nature* 499, 336–340.
- Chen, T.-W., Wardill, T.J., Sun, Y., Pulver, S.R., Renninger, S.L., Baohan, A., Schreiter, E.R., Kerr, R.A., Orger, M.B., Jayaraman, V., et al. (2013b). Ultrasensitive fluorescent proteins for imaging neuronal activity. *Nature* 499, 295–300.
- Chen, J.L., Voigt, F.F., Javadzadeh, M., Krueppel, R., and Helmchen, F. (2016). Long-range population dynamics of anatomically defined neocortical networks. *eLife* 5, e14679.
- Cisek, P., and Kalaska, J.F. (2010). Neural mechanisms for interacting with a world full of action choices. *Annu. Rev. Neurosci.* 33, 269–298.
- Cook-Snyder, D.R., Jones, A., and Reijmers, L.G. (2015). A retrograde adenovirus for collecting ribosome-bound mRNA from anatomically defined projection neurons. *Front. Mol. Neurosci.* 8, 56.
- Dana, H., Chen, T.W., Hu, A., Shields, B.C., Guo, C., Looger, L.L., Kim, D.S., and Svoboda, K. (2014). Thy1-GCaMP6 transgenic mice for neuronal population imaging in vivo. *PLoS ONE* 9, e108697.
- Deverman, B.E., Pravdo, P.L., Simpson, B.P., Kumar, S.R., Chan, K.Y., Banerjee, A., Wu, W.-L., Yang, B., Huber, N., Pasca, S.P., and Gradianaru, V. (2016). Cre-dependent selection yields AAV variants for widespread gene transfer to the adult brain. *Nat. Biotechnol.* 34, 204–209.
- Douglas, R.J., and Martin, K.A. (2007). Recurrent neuronal circuits in the neocortex. *Curr. Biol.* 17, R496–R500.
- Engel, A.K., Fries, P., and Singer, W. (2001). Dynamic predictions: oscillations and synchrony in top-down processing. *Nat. Rev. Neurosci.* 2, 704–716.
- Ferezou, I., Haiss, F., Gentet, L.J., Aronoff, R., Weber, B., and Petersen, C.C.H. (2007). Spatiotemporal dynamics of cortical sensorimotor integration in behaving mice. *Neuron* 56, 907–923.
- Fox, M.D., Snyder, A.Z., Vincent, J.L., Corbetta, M., Van Essen, D.C., and Raichle, M.E. (2005). The human brain is intrinsically organized into dynamic, anticorrelated functional networks. *Proc. Natl. Acad. Sci. USA* 102, 9673–9678.
- Frostig, R.D., Lieke, E.E., Ts'o, D.Y., and Grinvald, A. (1990). Cortical functional architecture and local coupling between neuronal activity and the microcirculation revealed by in vivo high-resolution optical imaging of intrinsic signals. *Proc. Natl. Acad. Sci. USA* 87, 6082–6086.
- Gilbert, C.D., and Li, W. (2013). Top-down influences on visual processing. *Nat. Rev. Neurosci.* 14, 350–363.
- Goard, M.J., Pho, G.N., Woodson, J., and Sur, M. (2016). Distinct roles of visual, parietal, and frontal motor cortices in memory-guided sensorimotor decisions. *eLife* 5, 1–30.
- Guo, Z.V., Li, N., Huber, D., Ophir, E., Gutnisky, D., Ting, J.T., Feng, G., and Svoboda, K. (2014). Flow of cortical activity underlying a tactile decision in mice. *Neuron* 81, 179–194.
- Harris, K.D., and Mrsic-Flogel, T.D. (2013). Cortical connectivity and sensory coding. *Nature* 503, 51–58.
- Hernández, A., Nácher, V., Luna, R., Zainos, A., Lemus, L., Alvarez, M., Vázquez, Y., Camarillo, L., and Romo, R. (2010). Decoding a perceptual decision process across cortex. *Neuron* 66, 300–314.

- Huang, Z.J., and Zeng, H. (2013). Genetic approaches to neural circuits in the mouse. *Annu. Rev. Neurosci.* 36, 183–215.
- Husson, T.R., Mallik, A.K., Zhang, J.X., and Issa, N.P. (2007). Functional imaging of primary visual cortex using flavoprotein autofluorescence. *J. Neurosci.* 27, 8665–8675.
- Kato, S., Kaplan, H.S., Schrödel, T., Skora, S., Lindsay, T.H., Yemini, E., Lockery, S., and Zimmer, M. (2015). Global brain dynamics embed the motor command sequence of *Caenorhabditis elegans*. *Cell* 163, 656–669.
- Katz, L.N., Yates, J.L., Pillow, J.W., and Huk, A.C. (2016). Dissociated functional significance of decision-related activity in the primate dorsal stream. *Nature* 535, 285–288.
- Kepecs, A., and Fishell, G. (2014). Interneuron cell types are fit to function. *Nature* 505, 318–326.
- Kim, C.K., Yang, S.J., Pichamoorthy, N., Young, N.P., Kauvar, I., Jennings, J.H., Lerner, T.N., Berndt, A., Lee, S.Y., Ramakrishnan, C., et al. (2016). Simultaneous fast measurement of circuit dynamics at multiple sites across the mammalian brain. *Nat. Methods* 13, 325–328.
- Klapoetke, N.C., Murata, Y., Kim, S.S., Pulver, S.R., Birdsey-Benson, A., Cho, Y.K., Morimoto, T.K., Chuong, A.S., Carpenter, E.J., Tian, Z., et al. (2014). Independent optical excitation of distinct neural populations. *Nat. Methods* 11, 338–346.
- Kobak, D., Brendel, W., Constantinidis, C., Feierstein, C.E., Kepecs, A., Mainen, Z.F., Qi, X.L., Romo, R., Uchida, N., and Machens, C.K. (2016). Demixed principal component analysis of neural population data. *eLife* 5, 1–37.
- Komiyama, T., Sato, T.R., O'Connor, D.H., Zhang, Y.-X., Huber, D., Hooks, B.M., Gabitto, M., and Svoboda, K. (2010). Learning-related fine-scale specificity imaged in motor cortex circuits of behaving mice. *Nature* 464, 1182–1186.
- Kramer, R.S., and Pearlstein, R.D. (1979). Cerebral cortical microfluorometry at isosbestic wavelengths for correction of vascular artifact. *Science* 205, 693–696.
- Kvitsiani, D., Ranade, S., Hangya, B., Taniguchi, H., Huang, J.Z., and Kepecs, A. (2013). Distinct behavioural and network correlates of two interneuron types in prefrontal cortex. *Nature* 498, 363–366.
- Ledberg, A., Bressler, S.L., Ding, M., Coppola, R., and Nakamura, R. (2007). Large-scale visuomotor integration in the cerebral cortex. *Cereb. Cortex* 17, 44–62.
- Lerner, T.N., Shlyansky, C., Davidson, T.J., Evans, K.E., Beier, K.T., Zalocusky, K.A., Crow, A.K., Malenka, R.C., Luo, L., Tomer, R., and Deisseroth, K. (2015). Intact-brain analyses reveal distinct information carried by SNc dopamine subcircuits. *Cell* 162, 635–647.
- Li, N., Chen, T.W., Guo, Z.V., Gerfen, C.R., and Svoboda, K. (2015). A motor cortex circuit for motor planning and movement. *Nature* 519, 51–56.
- Ma, Y., Shaik, M.A., Kozberg, M.G., Kim, S.H., Portes, J.P., Timerman, D., and Hillman, E.M. (2016). Resting-state hemodynamics are spatiotemporally coupled to synchronized and symmetric neural activity in excitatory neurons. *Proc. Natl. Acad. Sci. USA* 113, E8463–E8471.
- Madisen, L., Garner, A.R., Shimaoka, D., Chuong, A.S., Klapoetke, N.C., Li, L., van der Bourg, A., Niino, Y., Egolf, L., Monetti, C., et al. (2015). Transgenic mice for intersectional targeting of neural sensors and effectors with high specificity and performance. *Neuron* 85, 942–958.
- Makino, H., and Komiyama, T. (2015). Learning enhances the relative impact of top-down processing in the visual cortex. *Nat. Neurosci.* 18, 1116–1122.
- Miller, E.K., and Buschman, T.J. (2013). Cortical circuits for the control of attention. *Curr. Opin. Neurobiol.* 23, 216–222.
- Miller, E.K., and Cohen, J.D. (2001). An integrative theory of prefrontal cortex function. *Annu. Rev. Neurosci.* 24, 167–202.
- Mohajerani, M.H., Chan, A.W., Mohsenvand, M., LeDue, J., Liu, R., McVea, D.A., Boyd, J.D., Wang, Y.T., Reimers, M., and Murphy, T.H. (2013). Spontaneous cortical activity alternates between motifs defined by regional axonal projections. *Nat. Neurosci.* 16, 1426–1435.
- Oh, S.W., Harris, J.A., Ng, L., Winslow, B., Cain, N., Mihalas, S., Wang, Q., Lau, C., Kuan, L., Henry, A.M., et al. (2014). A mesoscale connectome of the mouse brain. *Nature* 508, 207–214.
- Ohki, K., Chung, S., Ch'ng, Y.H., Kara, P., and Reid, R.C. (2005). Functional imaging with cellular resolution reveals precise micro-architecture in visual cortex. *Nature* 433, 597–603.
- Peron, S.P., Freeman, J., Iyer, V., Guo, C., and Svoboda, K. (2015). A cellular resolution map of barrel cortex activity during tactile behavior. *Neuron* 86, 783–799.
- Peters, A.J., Chen, S.X., and Komiyama, T. (2014). Emergence of reproducible spatiotemporal activity during motor learning. *Nature* 510, 263–267.
- Petreanu, L., Gutnisky, D.A., Huber, D., Xu, N.L., O'Connor, D.H., Tian, L., Looger, L., and Svoboda, K. (2012). Activity in motor-sensory projections reveals distributed coding in somatosensation. *Nature* 489, 299–303.
- Pfeffer, C.K., Xue, M., He, M., Huang, Z.J., and Scanziani, M. (2013). Inhibition of inhibition in visual cortex: the logic of connections between molecularly distinct interneurons. *Nat. Neurosci.* 16, 1068–1076.
- Pinto, L., and Dan, Y. (2015). Cell-type-specific activity in prefrontal cortex during goal-directed behavior. *Neuron* 87, 437–450.
- Pisauro, M.A., Dhruv, N.T., Carandini, M., and Benucci, A. (2013). Fast hemodynamic responses in the visual cortex of the awake mouse. *J. Neurosci.* 33, 18343–18351.
- Pnevmatikakis, E.A., Soudry, D., Gao, Y., Machado, T.A., Merel, J., Pfau, D., Reardon, T., Mu, Y., Lacefield, C., Yang, W., et al. (2016). Simultaneous denoising, deconvolution, and demixing of calcium imaging data. *Neuron* 89, 285–299.
- Poort, J., Khan, A.G., Pachitariu, M., Nemri, A., Orsolic, I., Krupic, J., Bauza, M., Sahani, M., Keller, G.B., Mrsic-Flogel, T.D., and Hofer, S.B. (2015). Learning enhances sensory and multiple non-sensory representations in primary visual cortex. *Neuron* 86, 1478–1490.
- Rajasethupathy, P., Sankaran, S., Marshel, J.H., Kim, C.K., Ferenczi, E., Lee, S.Y., Berndt, A., Ramakrishnan, C., Jaffe, A., Lo, M., et al. (2015). Projections from neocortex mediate top-down control of memory retrieval. *Nature* 526, 653–659.
- Rajasethupathy, P., Ferenczi, E., and Deisseroth, K. (2016). Targeting neural circuits. *Cell* 165, 524–534.
- Ratzlaff, E.H., and Grinvald, A. (1991). A tandem-lens epifluorescence microscope: hundred-fold brightness advantage for wide-field imaging. *J. Neurosci. Methods* 36, 127–137.
- Robles, F.E., Chowdhury, S., and Wax, A. (2010). Assessing hemoglobin concentration using spectroscopic optical coherence tomography for feasibility of tissue diagnostics. *Biomed. Opt. Express* 1, 310–317.
- Roelfsema, P.R., Engel, A.K., König, P., and Singer, W. (1997). Visuomotor integration is associated with zero time-lag synchronization among cortical areas. *Nature* 385, 157–161.
- Rudy, B., Fishell, G., Lee, S., and Hjerling-Leffler, J. (2011). Three groups of interneurons account for nearly 100% of neocortical GABAergic neurons. *Dev. Neurobiol.* 71, 45–61.
- Shibata, T., Shimoyama, I., Ito, T., Abla, D., Iwasa, H., Koseki, K., Yamanouchi, N., Sato, T., and Nakajima, Y. (1997). The time course of interhemispheric EEG coherence during a GO/NO-GO task in humans. *Neurosci. Lett.* 233, 117–120.
- Siegel, M., Buschman, T.J., and Miller, E.K. (2015). Cortical information flow during flexible sensorimotor decisions. *Science* 348, 1352–1355.
- Sofroniew, N.J., Cohen, J.D., Lee, A.K., and Svoboda, K. (2014). Natural whisker-guided behavior by head-fixed mice in tactile virtual reality. *J. Neurosci.* 34, 9537–9550.
- Spellman, T.J., and Gordon, J.A. (2015). Synchrony in schizophrenia: a window into circuit-level pathophysiology. *Curr. Opin. Neurobiol.* 30, 17–23.
- Spors, H., and Grinvald, A. (2002). Spatio-temporal dynamics of odor representations in the mammalian olfactory bulb. *Neuron* 34, 301–315.

- Stirman, J.N., Smith, I.T., Kudenov, M.W., and Smith, S.L. (2016). Wide field-of-view, multi-region, two-photon imaging of neuronal activity in the mammalian brain. *Nat. Biotechnol.* 34, 857–862.
- Stuart, G.J., and Spruston, N. (2015). Dendritic integration: 60 years of progress. *Nat. Neurosci.* 18, 1713–1721.
- Swanson, L.W. (2000). Cerebral hemisphere regulation of motivated behavior. *Brain Res.* 886, 113–164.
- Thévenaz, P., Ruttimann, U.E., and Unser, M. (1998). A pyramid approach to subpixel registration based on intensity. *IEEE Trans. Image Process.* 7, 27–41.
- Vanni, M.P., and Murphy, T.H. (2014). Mesoscale transcranial spontaneous activity mapping in GCaMP3 transgenic mice reveals extensive reciprocal connections between areas of somatomotor cortex. *J. Neurosci.* 34, 15931–15946.
- Wechselblatt, J.B., Flister, E.D., Piscopo, D.M., and Niell, C.M. (2016). Large-scale imaging of cortical dynamics during sensory perception and behavior. *J. Neurophysiol.* 115, 2852–2866.
- Xiao, D., Vanni, M.P., Mitelut, C.C., Chan, A.W., LeDue, J.M., Xie, Y., Chen, A.C., Swindale, N.V., and Murphy, T.H. (2017). Mapping cortical mesoscopic networks of single spiking cortical or sub-cortical neurons. *eLife* 6, e19976.
- Yuste, R. (2015). From the neuron doctrine to neural networks. *Nat. Rev. Neurosci.* 16, 487–497.
- Zalocusky, K.A., Ramakrishnan, C., Lerner, T.N., Davidson, T.J., Knutson, B., and Deisseroth, K. (2016). Nucleus accumbens D2R cells signal prior outcomes and control risky decision-making. *Nature* 531, 642–646.
- Zhang, S., Xu, M., Kamigaki, T., Hoang Do, J.P., Chang, W.-C., Jenvay, S., Miyamichi, K., Luo, L., and Dan, Y. (2014). Selective attention. Long-range and local circuits for top-down modulation of visual cortex processing. *Science* 345, 660–665.
- Zingg, B., Hintiryan, H., Gou, L., Song, M.Y., Bay, M., Bienkowski, M.S., Foster, N.N., Yamashita, S., Bowman, I., Toga, A.W., and Dong, H.W. (2014). Neural networks of the mouse neocortex. *Cell* 156, 1096–1111.

## STAR★METHODS

## KEY RESOURCES TABLE

REAGENT or RESOURCE	SOURCE	IDENTIFIER
<b>Antibodies</b>		
Chicken polyclonal anti-GFP	Aves Lab	Cat#GFP-1020; RRID: AB_10000240
Rabbit polyclonal anti-Parvalbumin	Abcam	Cat#ab11427; RRID: AB_298032
Rabbit polyclonal anti-Somatostatin	Santa Cruz Biotechnology	Cat#sc-7819; RRID: AB_2302603
Donkey anti-chicken Alexa488	Jackson Immunoresearch	Cat#703-545-155; RRID: AB_2340375
Donkey anti-rabbit Cy3	Jackson Immunoresearch	Cat#711-165-152; RRID: AB_2307443
<b>Bacterial and Virus Strains</b>		
AAV2/8- CaMKII $\alpha$ ::Chrimson-p2A-mCherry	Stanford Gene Vector and Virus Core	N/A
AAV2/8- CaMKII $\alpha$ ::mCherry	Stanford Gene Vector and Virus Core	N/A
AAV-PHP.B-CaMKII $\alpha$ ::jRCaMP1b	This paper	N/A
AAV-PHP.B-EF1 $\alpha$ ::DIO-GCaMP6f	This paper	N/A
AAV-PHP.B-CAG::DIO-GCaMP6f	This paper	N/A
<b>Chemicals, Peptides, and Recombinant Proteins</b>		
Muscinol hydrobromide	Sigma-Aldrich	CAS: 18174-72-6
4'6-diamidino-2-phenylindole	Sigma-Aldrich	CAS: 28718-90-3
<b>Experimental Models: Organisms/Strains</b>		
Mouse: Thy1-GFP: Tg(Thy1-EGFP)MJrs	The Jackson Laboratory	JAX#007788
Mouse: VGlutT1-Cre; Slc17a7 <sup>tm1.1(cre)Hze</sup>	The Jackson Laboratory	JAX#023527
Mouse: ZtTa: Gt(ROSA)26Sor <sup>tm5(ACTB-tTA)Luo</sup>	The Jackson Laboratory	JAX#012266
Mouse: Camk2a-tTA : Tg(Camk2a-tTA)1Mmay	The Jackson Laboratory	JAX#003010
Mouse: Ai93: Igs <sup>tm93.1(tetO-GCaMP6f)Hze</sup>	H. Zeng, Allen Institute for Brain Science	JAX#024103
Mouse: Thy1-GCaMP6f : Tg(Thy1-GCaMP6f)GP5.5Dkim	The Jackson Laboratory	JAX#024276
Mouse: SST-Cre; Sst <sup>tm2.1(cre)Zjh</sup>	The Jackson Laboratory	JAX#013044
Mouse: PV-Cre; Pvalb <sup>tm1(cre)Arbr</sup>	The Jackson Laboratory	JAX#008069
Mouse: VGAT-ChR2: B6.Cg-Tg(Slc332a1-COP4*H134R/EYFP)8Gfng/J	The Jackson Laboratory	JAX#014548
<b>Recombinant DNA</b>		
pAAV-CAG::DIO-GCaMP6f	This paper	N/A
pAAV-CaMKII $\alpha$ ::jRCaMP1b	This paper	N/A
<b>Software and Algorithms</b>		
Image registration, signal extraction, and analysis tools for two-photon and widefield data.	This paper	N/A
Two-photon trace deconvolution software.	Pnevmatikakis et al., 2016	N/A
TurboReg	Thévenaz et al., 1998	N/A

## CONTACT FOR REAGENT AND RESOURCE SHARING

Further information and requests for reagents may be directed to and will be fulfilled by the Lead Contact, Dr. Karl Deisseroth ([deissero@stanford.edu](mailto:deissero@stanford.edu)).

## EXPERIMENTAL MODEL AND SUBJECT DETAILS

All procedures were in accordance with protocols approved by the Stanford University Institutional Animal Care and Use Committee (IACUC) and guidelines of the National Institutes of Health. The investigators were not blinded to the genotypes of the animals, and all mice of the desired genotype were used for experiments. Both male and female mice were used, aged 6–10 weeks at time of surgery. Mice were group housed in plastic cages with disposable bedding on a standard light cycle until surgery, when they were split into

individual cages and moved to a 12 hr reversed light cycle. Following recovery after surgery, mice were water restricted to 1 mL/day. All experiments were performed during the dark period. The mouse strains used were *Tg(Thy1-EGFP)MJs* (Thy1-GFP, JAX#007788), *Gad2<sup>tm2(cre)Zjh</sup>* (Gad2-Cre, JAX#010802), *Slc17a7<sup>tm1.1(cre)Hze</sup>* (VGluT1-Cre, JAX#023527), *Gt(ROSA)26Sor<sup>tm5(CTB-tTA)Luo</sup>* (ZtTA, JAX#012266), *Tg(Camk2a-tTA)1Mmay* (Camk2a-tTA, JAX#003010), and *Igs7<sup>tm93.1(tetO-GCaMP6f)Hze</sup>* (Ai93, JAX#024103) (gift of H. Zeng, Allen Institute for Brain Science), *Tg(Thy1-GCaMP6f)GP5.5Dkim* (Thy1-GCaMP6f, JAX#024276), *Sst<sup>tm2.1(cre)Zjh</sup>* (SST-Cre, JAX#013044), *Pvalb<sup>tm1(cre)Arbr</sup>* (PV-Cre, JAX#008069), and *B6.Cg-Tg(Slc33a1-COP4\*H134R/EYFP)8Gfn* (VGAT-CR2, JAX#014548), all bred in a mixed C57BL6/J and CD1 background. Mice homozygous for Ai93 and heterozygous for the Cre and tTA transgenes were bred to produce triple transgenic mice with the genotypes Gad2-Cre;ZtTA;Ai93 and VGluT1-Cre;Camk2a-tTA;Ai93.

## METHOD DETAILS

### Animal behavior

A microcontroller-based real-time behavioral system (Bpod, built using an Arduino Due) was used to control delivery of stimuli, water reward, and air puff punishment. Licks were detected with a custom lickometer built using a capacitive touch sensor (Sparkfun) and a microcontroller (Arduino). For olfactory stimuli, an olfactometer was constructed using pure odorants (ethyl acetate and 2-pentanone, Sigma) diluted to 4% v/v in paraffin oil (Sigma). After waiting at least a week after surgery, mice were water restricted to 1 mL/day while maintaining > 80% pre-deprivation weight. After several days of handling and habituation to head fixation, mice were trained to lick for free reward (~2–3 µl). Once mice could reliably lick for water, they were started on a shaping protocol that automatically provided water reward (2–3 µl) 500 ms after the offset of either odor (delivered for 1 s). Once mice began reliably licking during the odor cue (1–2 days), they were imaged during training. During training, odors were delivered for 1 s, followed by 500 ms of no stimulus, then a 1 s response window. Licking within the response window on GO trials was rewarded with a water droplet. Licking during the No-Go trials was punished with an airpuff to the face. Airpuffs (100 ms, 10 psi) were delivered via a solenoid valve (NResearch) attached to a P1000 pipette. Mice typically began withholding licks during No-Go trials within 80 trials.

### Two-photon imaging

A 7 mm window (Menzel-Gläser) was implanted over a craniotomy, compressing the brain lightly, and a custom headbar was affixed. Mice were allowed to recover for at least 1 week before being water restricted and trained on the task. Mice stably performing the olfactory discrimination task (> 70% trials/session correct) were imaged using a two-photon microscope (Bruker Ultima) with an Olympus 25X/1.05NA objective. Clear ultrasound gel was used as an immersion medium (Aquasonic, Parker Laboratories). Before each two-photon imaging session, an Olympus 2X/0.14NA objective and a pco.edge 5.5 sCMOS camera were used to capture an epi-illuminated one-photon widefield calibration image of the entire window, with the translation stage holding the mouse centered at its origin.

### Widefield imaging

Mice were anesthetized with isoflurane, the scalp was removed, skull cleaned and dried, and custom head-plate was cemented to contacts over the cerebellum and in front of the olfactory bulb. The skull was then covered in a thin layer of cyanoacrylate glue (Apollo 2000, Cyberbond), clear dental acrylic (Ortho-Jet, Lang Dental), and clear nail polish (Electron Microscopy Services) (Guo et al., 2014). Buprenorphine (0.1 mg/kg) was injected subcutaneously at end of surgery. Mice were given > = 1 wk recovery before experiments. Imaging was performed on a custom-built fluorescence macroscope designed for high light collection efficiency and large field of view. The macroscope consisted of back-to-back 50 mm f/1.2 camera lenses (Nikon), separated by a FF495-Di03-50.8-D dichroic mirror (Semrock), mounted in a 60 mm cube (Thorlabs). An F-mounted ORCA Flash 4.0 (Hamamatsu) was used to record images, with a FF01-520/35-50.8-D emission filter (Semrock). Alternating 410nm and 488nm illumination for non-calcium dependent artifact removal was controlled using a microcontroller (Arduino) slaved to the frame output trigger of the camera.

### Local inactivation experiments

For optogenetic inhibition experiments, VGAT-ChR2 mice were prepared using the same preparation as for widefield imaging, and then trained on the olfactory Go/No-Go task until near perfect performance. The 473 nm laser illumination was controlled by a microcontroller (Arduino) and coupled into a fiber optic splitter. Continuous wave laser illumination was used, with 20 mW at output of each fiber tip (Goard et al., 2016). Fibers were positioned over the brain using micromanipulator translation stages, with coordinates calibrated to bregma for each mouse. For pharmacological inhibition experiments, 250 nL of 1 µg/µl muscimol hydrobromide (Sigma) in saline was bilaterally injected into ALM (2.4 mm anterior, 2.0 mm lateral to bregma), or somatosensory cortex (~1 mm posterior, 3.2 mm lateral to bregma) of well-trained Thy1-GCaMP6f mice. This injection volume and concentration of muscimol were chosen based on previous studies inactivating small parts of cortex (Pinto and Dan, 2015). Following surgery, mice were allowed at least an hour for recovery before imaging. The skull was covered with silicone elastomer between imaging sessions.

### Widefield Imaging (detailed description)

Imaging was performed on a custom-built fluorescence macroscope designed for high light collection efficiency and large field of view. Images were collected after focusing ~500 µm below the surface of the most dorsal point on the skull, in order to focus

past surface blood vessels. The macroscope consisted of back-to-back 50 mm f/1.2 camera lenses (Nikon), separated by a FF495-Di03-50.8-D dichroic mirror (Semrock), mounted in a 60 mm cube (Thorlabs). An F-mounted ORCA Flash 4.0 (Hamamatsu) was used to record images, with FF01-520/35-50.8-D emission filter (Semrock). To increase sensitivity and decrease data quantity, pixels were binned 4x4. Illumination light was provided by a pair of high power, temperature-stabilized 405 nm and 470 nm LEDs (Cairn Research). The 405 nm and 470 nm LEDs were then filtered with a FB410-10 and FL488-3 filter respectively, and joined by a DMLP425L longpass dichroic mirror (Thorlabs) and coupled into the 60 mm cube with a third 50 mm f/1.2 camera lens (Nikon). Parts list and diagram available on request. For simultaneous RCaMP/GCaMP imaging, a Dual View Lambda (Photometrics) image splitter containing a FF555-Di03-25x36 dichroic and FF01-520/15-25 (GCaMP) and FF02-617/73-25 (RCaMP) emission filters (Semrock) was inserted immediately before the camera sensor. A FF410/504/582/669-Di01-50-D dichroic was used between the lenses of the macroscope, and a 560 nm LED (Cairn Research), filtered by a FF01-560/14-25 (Semrock) was added into the existing illumination path using a FF520-Di02-50.8 longpass dichroic.

### Stimulus Delivery

A microcontroller-based real time behavioral system (Bpod, built using an Arduino Due) was used to control stimulus delivery through a DAQ card (National Instruments). For auditory stimuli, the NIDAQ output a 15 kHz sine wave analog signal to an electrostatic speaker calibrated to output at 70 db (EC1, TDT). For visual stimuli, the Bpod output through an Arduino to flash a green LED (TinkerKit, Arduino), which was shielded from the macroscope using black tape. For tactile stimuli, the NIDAQ output a 10 Hz sine wave through a linear amplifier (EPA-008-1, Piezo Systems) to a 4-layer piezoelectric bending actuator (T434-A4-302, Piezo Systems) which was placed against the mouse's whiskers.

### Widefield Image Registration

A 2D top-projection atlas was generated from the annotated Allen Brain Atlas volume, version CCFv2, in MATLAB (MathWorks). Videos were registered to this atlas using an affine transformation computed from four control points that were selected manually: the anterior tip of the olfactory bulb, the center of the suture at the base of retrosplenial cortex, and the left and right base of the olfactory bulb. This registration process was verified to be accurate and reproducible based on the visual, auditory, and tactile stimuli data that each aligned with the corresponding cortical region.

### Olfactory Behavioral Setup

Licks were detected with a custom lickometer built using a capacitive touch sensor (Sparkfun) and a microcontroller (Arduino). The input to the touch sensor was soldered to a lick port (Popper animal feeding needle). Water was delivered by a gravity-assisted syringe attached to the lickometer, and controlled by a quiet solenoid valve (Lee Valve). Pure odorants (ethyl acetate and 2-pentanone, Sigma) were diluted to 4% v/v in paraffin oil (Sigma) and pressurized with air (1 L/min). Two 3-way valves (NResearch), with the normally open port connected to a blank vial and the normally closed port connected to an odor vial, controlled odor delivery. Odor delivery was controlled by actuating solenoid valves to switch airflow away from a blank valve and to the odor valve. Odors were delivered through a Teflon tube placed ~1 cm from the mouse's nose. All valve openings were controlled with Bpod, which also recorded the time of licks, and synchronized odor timing with the camera.

### Histology and Immunohistochemistry

Mice were euthanized with beuthanasia, then transcardially perfused with ice-cold saline followed by 4% paraformaldehyde (PFA) (Electron Microscopy Sciences). After overnight fixation in 4% PFA, 100 µm sagittal sections were cut on a vibratome (Leica). For the immunostaining in [Figure 3](#), sections were blocked for 2 hr in 10% normal donkey serum (NDS) + 0.3% Triton X-100 in PBS (PBST), and then stained overnight at 4°C in 5% NDS + 0.3% PBST with a primary antibody, either parvalbumin (Abcam ab11427, 1:1000) or somatostatin (Santa Cruz sc-7819, 1:500) and GFP (Aves GFP-1020, 1:1000). After three washes in 0.3% PBST, sections were stained with secondary anti-rabbit Cy3 (1:500) and anti-chicken Alexa488 (1:500) antibodies (Jackson ImmunoResearch) for at least 3 hr. After three more washes, the sections were then stained with 4'6-diamidino-2-phenylindole (DAPI) for 15 min and mounted with Vectashield (Vectorlabs). Widefield images of sagittal sections were taken using the same custom macroscope used for *in vivo* imaging, and confocal images were taken on either a Leica TCS SP5 ([Figure 1](#)) or a Zeiss LSM 780 ([Figure 3](#)) microscope.

### AAV-PHP.B Production and Intravenous Administration

AAV-PHP.B was produced using PEI-mediated triple transfection of HEK293 cells, following the protocol described in Deverman et al., 2016. After transfection, media containing virus was harvested once at 72 hr and once again at 120 hr, when the cells were harvested as well. Cells were lysed using multiple freeze/thaw rounds, and free virus was precipitated from the media using PEG then added to the cell lysate. Extra-viral DNA was digested using Salt Active Nuclease, and the virus was purified using an iodixanol step gradient and concentrated. AAV was titered using standard qPCR methods. 50–100 µl of virus (corresponding to 1E12 vg) was injected retro-orbitally using a 0.5 mL insulin syringe, and at least four weeks were allowed for expression before imaging.

### Optogenetic Inactivation Experiments

VGAT-Chr2 mice were prepared using the same preparation as for widefield imaging, and then trained on the Olfactory Go/No-Go task until near perfect performance (minimum 70% correct, although all mice ended up performing above 90%). Coupling a 473 nm laser to a 2x2 fiber splitter (Thorlabs FCMH2-FCL), each output fiber was held with a fiber clamp (Thorlabs FCM), and positioned independently using micromanipulator translation stages, with coordinates calibrated to bregma for each mouse. The laser was controlled by a microcontroller (Arduino), stimulating during the cue through reward period of a random subset of trials as the mice performed the task for 100 trials per inhibited region. Continuous laser illumination was used, with 20 mW at output of each fiber tip. Data was acquired across multiple sessions across multiple days.

### Muscimol Inactivation Experiments

Muscimol hydrobromide (Sigma) was dissolved in saline to a concentration of 1  $\mu$ g/ $\mu$ L. A small ~500  $\mu$ m craniotomy was drilled over ALM (2.4 mm anterior, 2.0 mm lateral to bregma, or somatosensory cortex (~1 mm posterior, 3.2 mm lateral to bregma) of trained Thy1-GCaMP6f mice. 250 nL of muscimol or saline were injected using a pulled glass pipette backfilled with oil at a rate of 100 nL/min. The injected substance was allowed to diffuse for 2–3 min, and then the pipette was withdrawn. This injection volume and concentration of muscimol were chosen based on previous studies inactivating small parts of cortex (Pinto and Dan, 2015). Following surgery, mice were allowed at least an hour for recovery before imaging. The skull was covered with silicone elastomer between imaging sessions.

### Optogenetic Activation

We injected Thy1-GCaMP6f mice bilaterally with 400 nL of CaMKII $\alpha$ ::Chrimson-p2A-mCherry or CaMKII $\alpha$ ::mCherry packaged in AAV8 (both ~1E13 vg/ml, Stanford Gene Vector & Virus Core). Mice were simultaneously prepared with a headbar and clear skull cap for imaging. After waiting one week for expression, in these naive untrained mice, we used our macroscope to image neural activity while bilaterally stimulating ALM using a fiber-coupled 594 nm laser triggered by an Arduino, at 10 Hz with 10 ms pulses. Fibers were positioned over ALM. Power at the tip of each fiber ranged between 2–7 mW depending on the level of viral expression and the quality of the clear skull preparation, calibrated so as to achieve a licking response. Tongue movements were recorded using a mono-chrome Manta G-032 B camera (Allied Vision Tech). At least 10 stimulation trials were recorded for each mouse, each 4 s in duration, and separated by a variable intertrial interval of at least 10 s. Timing of stimulation, Manta recording, and macroscope recording were synchronized using a DAQ card (National Instruments).

### Two-photon Imaging

An approximately seven millimeter craniotomy was made centered on the midline of the mouse's skull, stretching from ~4 mm anterior to bregma to just anterior to the lambda suture. The brain was rinsed with sterile saline to remove blood, and a 7 mm window (Menzel-Gläser) was implanted over the craniotomy, compressing the brain lightly. The interface between the skull and window was filled with VetBond (3M), and then the window was sealed in place with a layer of Metabond (Parkell). Mice were allowed to recover for at least 1 week before being water restricted and trained on the task. Mice stably performing the olfactory discrimination task (> 70% trials/session correct) were imaged using a two-photon microscope (Bruker Ultima) with an Olympus 25X/1.05NA objective. Clear ultrasound gel was used as an immersion medium (Aquasonic, Parker Laboratories). Before each two-photon imaging session, an Olympus 2X/0.14NA objective and a pco.edge 5.5 sCMOS camera were used to capture an epi-illuminated one-photon widefield calibration image of the entire window, with the translation stage holding the mouse centered at its origin. For each behavioral trial, at least 180 single-plane images (256  $\times$  256 pixels) were acquired at 30 Hz, synchronized at the start of each trial using a TTL output from the Bpod behavior controller, while frame acquisition times were recorded with Bpod. Each session consisted of at least 30 trials, with equal numbers of Go and No-Go trials.

## QUANTIFICATION AND STATISTICAL ANALYSIS

### Statistical analysis

The target number of subjects used in each subject was determined based on numbers in previous published studies. Mean  $\pm$  s.e.m. was used to report statistics. The statistical test used and the definition  $N$  for each analysis is listed in the Results text and figure legends; non-parametric tests were used wherever appropriate. Significance was defined as  $\alpha = 0.05$ . Multiple comparisons were corrected for by Bonferroni or Benjamini-Hochberg correction. No statistical methods were used to pre-determine sample size, or to randomize. Animals were excluded prior to the collection of experimental data based on surgery quality. Statistical tests were performed in MATLAB (MathWorks). Variances were checked for similarity between each group.

### Widefield analysis

Analysis was performed using custom MATLAB (MathWorks) code. Videos were registered to a 2D top-projection atlas generated from the annotated Allen Brain Atlas volume, version CCFv2, in MATLAB (MathWorks), using an affine transformation computed from four manually selected control points. Each video was  $\Delta F/F$  normalized, using the median for each pixel over the entire time series as  $F$ . The 410 nm channel was then temporally smoothed using a moving average (width = 400 ms). The smoothed 410 nm  $\Delta F/F$

signal for each pixel was regressed onto the 488nm  $\Delta F/F$  signal for the corresponding pixel, and the regression coefficients were used to scale the 410 nm channel to the 488 nm channel. This scaled 410 nm  $\Delta F/F$  signal was then subtracted from the 488 nm  $\Delta F/F$  signal to produce a normalized signal for each pixel. For quantification, activity traces were extracted from points centered in six cortical regions (auditory, visual, somatosensory, parietal, motor, retrosplenial) on the left hemisphere of the brain.

### Two-photon analysis

Two-photon tiff stacks were denoised using the PureDenoise ImageJ plug-in (global noise estimation, 3 cycle spins) and then registered to the average image using the TurboReg ImageJ plug-in using rigid body transformations. Cellular region of interests (ROIs) were semi-automatically selected, based on [Rajasethupathy et al. \(2015\)](#), and manually verified. Contaminating neuropil signal was estimated from an annulus surrounding each soma mask and removed. The contaminating signal from the surrounding neuropil was removed using the function  $F(t) = F_{\text{soma}}(t) - 0.7 * F_{\text{neuropil}}(t)$  ([Chen et al., 2013b](#)), where  $F_{\text{soma}}(t)$  is the somatic  $\Delta F/F_0$  and  $F_{\text{neuropil}}(t)$  is the  $\Delta F/F_0$  from an annulus 4 pixels wide surrounding each soma mask, and including only pixels with a fluorescence standard deviation at least less than two times the standard deviation of the somatic trace ([Peters et al., 2014](#)).  $\Delta F(t)/F_0 = (F(t)-F_0)/F_0$  was computed as using the running 20<sup>th</sup> percentile average over a 10 s timewindow for  $F_0$ . The resulting  $\text{Ca}^{2+}$  traces were then processed using a Markov chain Monte Carlo-based algorithm to produce a de-noised, event-based activity trace ([Pnevmatikakis et al., 2016](#)). The full frame fluorescence was computed by summing all of the pixels in each frame on each time point, and then computing  $\Delta F/F_0$  the same way. Imaged fields of view were registered across mice. Peaks in cellular two-photon traces had a median signal-to-noise ratio (SNR), across cells and multiple fields of view, of 13, ranging from 4 to 24, with a median  $\Delta F/F_0$  noise of 0.03. Noise was calculated as the standard deviation of the raw  $\Delta F/F_0$  signal minus the de-noised  $\Delta F/F_0$  signal. Signal magnitude was computed as the mean value of all peaks that were greater than three standard deviations above the noise. SNR was then computed as signal magnitude divided by noise. Cells that were determined to be task-selective were used for subsequent analysis. Task-selective cells were defined as cells that fired significantly more during the task than during the baseline period, with significance determined by comparison to a bootstrapped null distribution of cell activity shuffled in time.

The location of each two-photon field of view relative to the calibration image was calculated using a fixed, calibrated linear mapping between translation stage XY coordinates and sCMOS camera pixel coordinates. Calibration images (and thus field of view locations) were then registered across sessions using manual keypoints.

### Clustering Analysis

To analyze the different response types of neurons, we applied unsupervised hierarchical clustering with complete linkage to the first 3 principal component loadings across cells (comprising > 95% of the variance), computed by performing PCA on average timeseries of individual cells on Hit trials. Manual inspection of running the algorithm with different numbers of clusters revealed that five clusters best fit our qualitative assessment of response categories.

### ROC Analysis

This analysis sought to distinguish between Go and No-Go trials based on the activity of each cell or cortical region in each trial ([Chen et al., 2013a](#)). Classification was based on a comparison of the  $\text{Ca}^{2+}$  transient from each cell or cortical region during the 2 s following odor onset to the mean trace during that time window for that cell or cortical region on either Hit or Correct Reject trials. Each trial was assigned a ‘discrimination variable’ (DV) equal to the dot product between the activity trace on that trial and the difference between the mean activity trace on all other trials of that type except for that trial, and the mean activity trace on all trials of the other type. Trial type was assigned based on whether the DV was greater than a criterion value. An ROC (receiver operating characteristic) curve was computed by systematically varying this criterion value, and computing the probability that either Hit (x axis) or Correct Reject (y axis) trial exceeded that criterion value. The area under this curve was then computed to find the fraction of trials on which an ideal observer could discriminate trial type using the DV. To find the chance performance for each neuron, the trial labels were shuffled 1000 times and the percent correctly discriminated was computed. Only cells whose performance was greater than the mean of 95<sup>th</sup> percentile of this shuffled distribution were plotted in [Figure 2A](#).

### Model-based Analysis

We created a GLM to predict each cell’s denoised  $\Delta F/F$  trace from a collection of input variables representing progression of the task and licking in a given trial. For every trial, we parameterized the task progression and licking behavior with a matrix of indicator variables. Indicator variables representing the task were constructed such that a single variable was provided for the occurrence of every time frame from odor onset to the end of the reward period (with an 100ms time window), and had a value of 1 200ms preceding its respective time frame and 0 otherwise. Indicator variables representing licking modeled lick onset, lick bout, and lick offset, such that a single variable represented a single time frame in which licking onset, lick bout, or lick offset occurred. These variables were 1 300ms preceding the occurrence of the corresponding lick frame and 0 otherwise. Licking was modeled only if it occurred 2 s after a previous bout. While variables representing the task progression were constant for every trial, variables representing the licking behavior varied across trial. We trained a GLM for each cell by concatenating parameterized input matrices for a subset of trials

and fitting the corresponding vector of parameters using ridge regression to concatenated  $\Delta F/F$  traces for the corresponding trials. We then evaluated our model by predicting traces of held out test trials, retaining only those models whose predictions were deemed significant by bootstrapping.

#### **Sources and mitigation of non $\text{Ca}^{2+}$ -dependent signals (related to Figure 3)**

There are a number of potential artifact sources in widefield calcium imaging, including movement, bleaching, and autofluorescence. We minimized movement artifacts by using a stainless steel headbar that had contact points both above the cerebellum and anterior to the olfactory bulb to ensure that the entire skull was rigidly fixed. Although brain movement within a fixed skull is often problematic for cellular resolution imaging, in our two-photon cellular resolution datasets brain motion was generally on the order of tens of microns. Because the spatial resolution of widefield imaging is more mesoscopic (on the order of hundreds of microns), motion should therefore not be a primary source of artifacts. Bleaching was also not apparent at the power densities used.

However, as we did observe artifactual signal in Thy1-GFP control mice (which should have no calcium dependent signal), we determined that the most prominent artifacts were likely due to autofluorescence and hemodynamic absorption (Vanni and Murphy, 2014). In order to distinguish between calcium-dependent signal and non-calcium-dependent artifacts, we used illumination multiplexing. Previous work has shown that when excited with 410 nm light as opposed to 488 nm light, the fluorescence emission of GCaMP is essentially calcium-independent (Lerner et al., 2015; Zalocusky et al., 2016). Further, the ratio of absorption of oxygenated versus deoxygenated hemoglobin is nearly identical at those wavelengths (1.535 versus 1.52) (Robles et al., 2010), and both wavelengths fall within the flavoprotein autofluorescence excitation spectrum, which fluoresces linearly with the concentration of flavoprotein (Husson et al., 2007). By using 410 nm and 488 nm light, we could maintain a fully epifluorescent, dichroic-based illumination system, in contrast to reflectance based hemodynamic measurement techniques that use off-axis illumination that requires a more ad hoc optical system (Wekselblatt et al., 2016). Additionally, with this approach, we directly measure the effect on emitted fluorescence of these as well as other, potentially undiagnosed, noise sources.

We recorded complementary, interleaved 15 Hz videos by alternating illumination every other camera frame. After demultiplexing, we used the calcium-independent signal to mitigate non-GCaMP related artifacts in the calcium-dependent signal. There is precedent in the literature for both linear (Frostig et al., 1990; Kim et al., 2016; Spors and Grinvald, 2002; Wekselblatt et al., 2016) and divisive (Akemann et al., 2012; Kramer and Pearlstein, 1979) approaches to removing background signal in optically recorded non-single cell resolution neural data. Both are effective because, approximated by a first order Taylor expansion, they are equivalent. In particular,  $F_{\text{corrected}} = F_c = F / R_m = [F_0 (1 + \Delta F)] / [R_{m0} (1 + \Delta R_m)] \approx [F_0 / R_{m0}] (1 + \Delta F) (1 - \Delta R_m)$ , and thus  $\Delta F_c = [R_{m0} / F_0] F_c - 1 \approx \Delta F - \Delta R_m$ , where  $F$  is the calcium-dependent signal;  $F_0$  is the baseline signal;  $\Delta F = [F - F_0] / F_0$ ;  $F_c$  is the corrected signal; and  $R_m$  is the multiplicative calcium-independent signal (Wekselblatt et al., 2016) and  $F_{c0} = F_0 / R_{m0}$ . Further, because there are also additive noise terms, specified as  $R_a$ , including background and autofluorescence, we ultimately wanted to compute  $\Delta F_c \approx \Delta F - \alpha \Delta R_m - \beta \Delta R_a$  where  $\alpha$  and  $\beta$  are (unknown) scaling factors that represent the different relative signal strengths in the single measured calcium-independent recording channel. To approximate these factors, before subtraction, we low-pass filtered  $\Delta R$  to remove high frequency noise that is uncorrelated with the calcium-dependent signal, and then scaled  $\Delta R$  to minimize the sum of squared difference with  $\Delta F$ , thus removing the overall calcium-independent component of  $\Delta F$ . We empirically tested both additive and divisive approaches using spontaneous data from Thy1-GFP mice, which should exhibit no calcium-dependent signal. We found that both approaches offered similar performance for mitigating background artifacts, although subtraction performed better and more consistently. We hypothesize that this results from the fact that the background is a mixture of both additive and multiplicative factors, as well as the higher susceptibility of a divisive approach to magnifying additive noise that is also present in the calcium-independent signal.

**Supplemental Information**

**Global Representations of Goal-Directed Behavior  
in Distinct Cell Types of Mouse Neocortex**

**William E. Allen, Isaac V. Kauvar, Michael Z. Chen, Ethan B. Richman, Samuel J. Yang, Ken Chan, Viviana Gradinaru, Benjamin E. Deverman, Liqun Luo, and Karl Deisseroth**

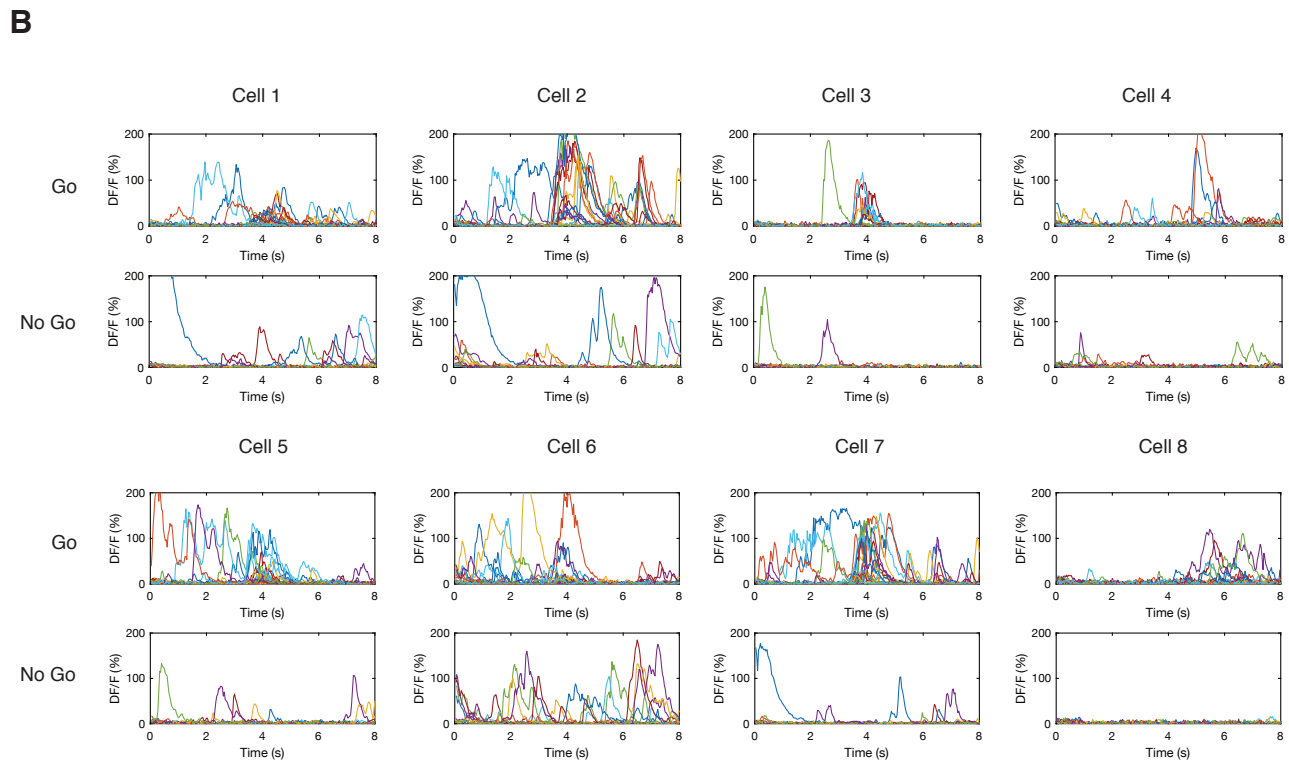
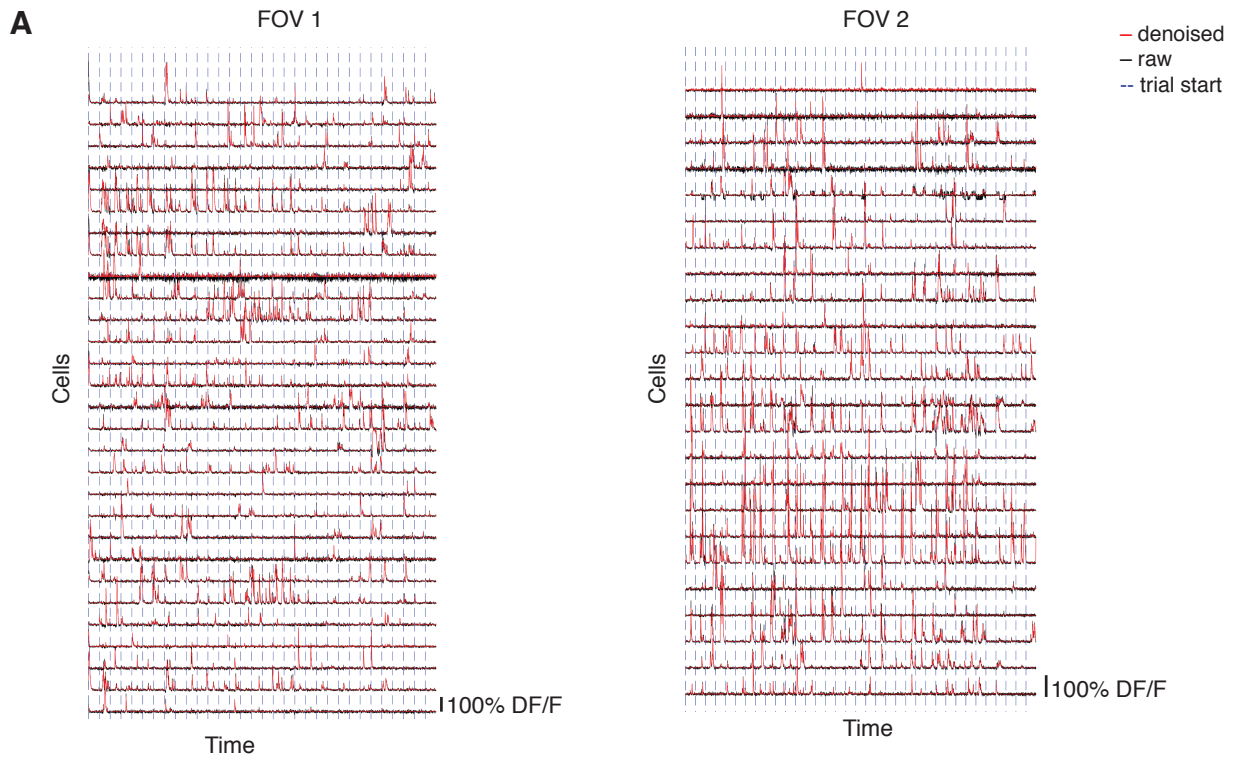


**Figure S1. Example single cell two-photon data (related to Figure 1).** (A) Representative example traces of all cells from two fields of view in two mice. Trial start times, including both Go and No-Go trials, are indicated with dashed blue lines, raw  $\Delta F/F$  normalized data as the black trace, and denoised  $\Delta F/F$  trace as the red trace. (B) Representative denoised  $\Delta F/F$  normalized traces from eight cells separately overlaid in different colors from single Go and No-Go trials, showing that some cells tend to reliably become activated during a specific point in Go trials.

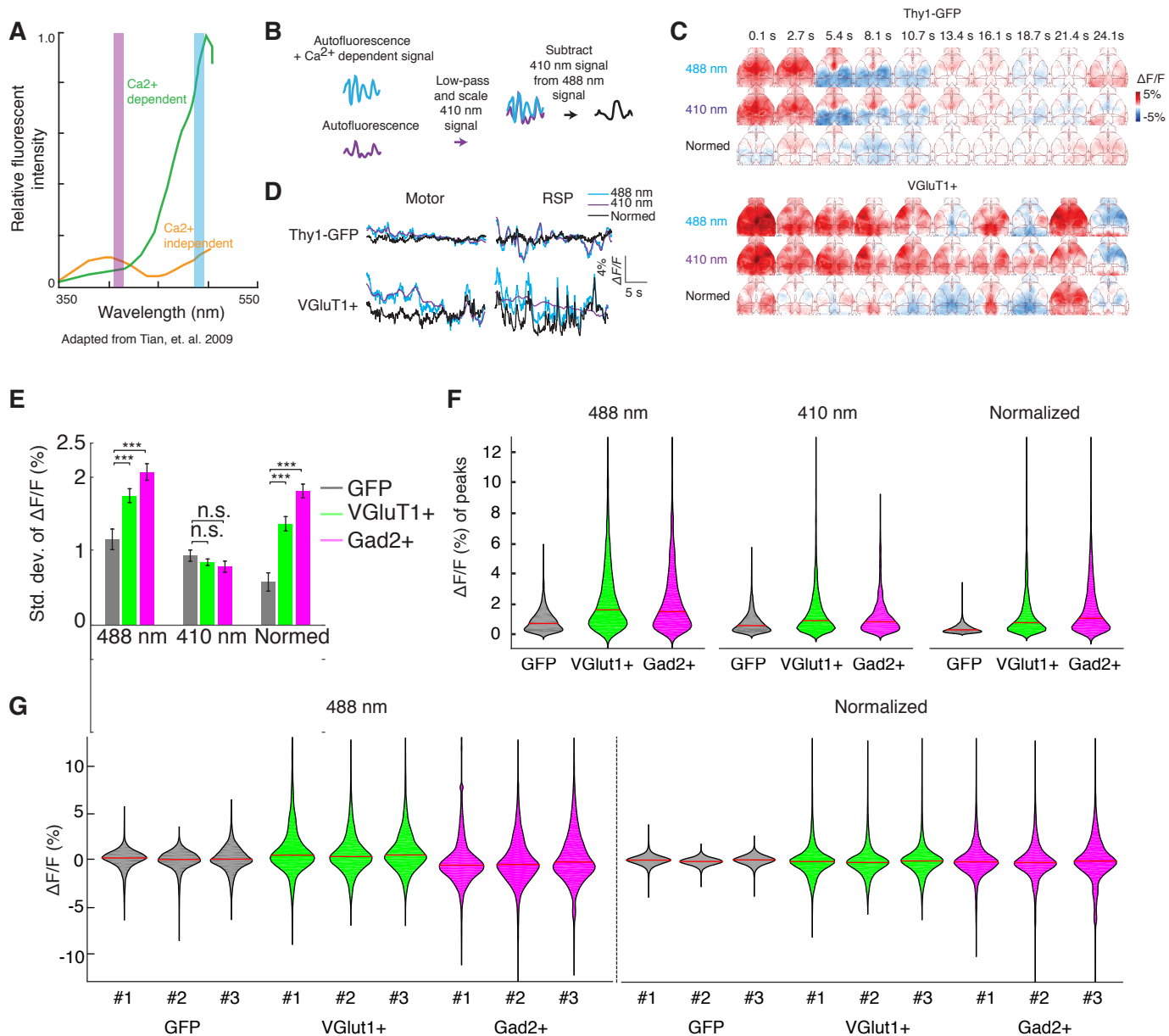


**Figure S2. Blood artifact reduction with spectral unmixing (related to Figure 3).** (A) Spectra of Ca<sup>2+</sup> dependent (green) and Ca<sup>2+</sup> independent (orange) GCaMP absorption. The absorption of the two states at 410 nm is nearly identical. (B) Schematic of subtractive normalization procedure, which assumes that auto fluorescence and artifacts are additive on to GCaMP fluorescence. (C) Top: Spontaneous fluorescence changes in control Thy1-GFP mouse under 488 nm and 410 nm illumination, and normalized fluorescence. Bottom: Spontaneous fluorescence changes in VGlut1+ triple transgenic mouse, under 488 nm and 410 nm illumination, and normalized fluorescence. (D) Example traces from (C) in motor and visual cortex. (E) Comparison of mean standard deviation across 1 minute trials, in each fluorescence channel and after normalization. N = 3 GFP, N = 3 Gad2, and N = 3 VGlut1+ mice, 10 trials for each mouse. Mean standard deviation for GFP mice is <0.5% ΔF/F, and therefore any normalized signals >1% ΔF/F should be reliable with a 95% confidence interval. In general, normalized signals for GCaMP expressing mice > 2-3% ΔF/F during behavior. (F) Distribution of the value of peaks in the spontaneous time series used in (E), with 488 nm and 410 nm illumination, and normalized. (G) Distribution of fluorescence change (% ΔF/F) values for all mice used in the comparison, before and after normalization.

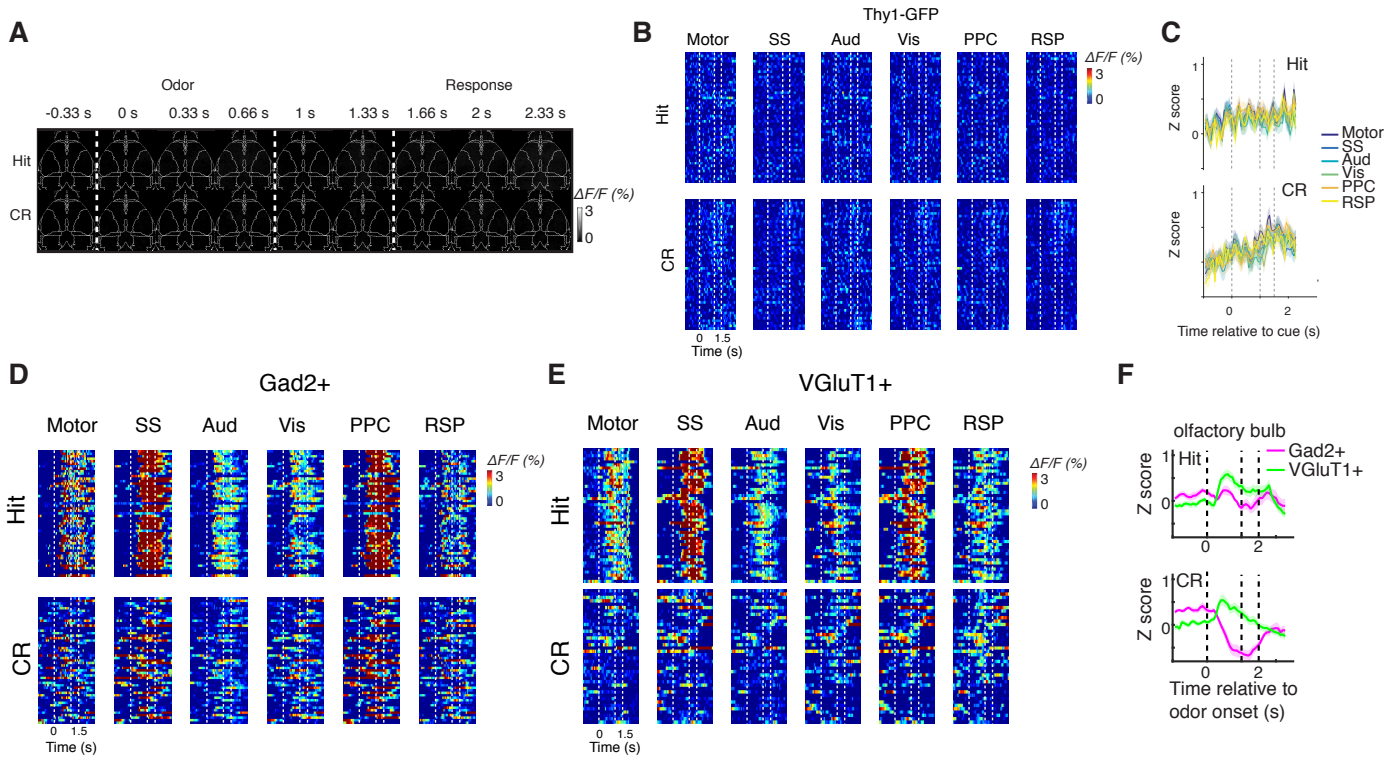


**Figure S3. GFP control during learned behavior, consistency of per-trial activity, and olfactory bulb traces (related to Figure 4).** (A) Example trial-averaged video sequence in Thy1-GFP mouse performing an olfactory discrimination task. (B) Single trial activity across multiple cortical areas from representative Thy1-GFP in (A). (C) Average traces in six cortical regions across  $N = 3$  Thy1-GFP mice. Mean  $\pm$  s.e.m. (D) Single-trial data from one Gad2+ mouse across multiple cortical regions over one behavioral session. (E) Single-trial data from one VGluT1+ mouse across multiple cortical regions over one behavioral session. (F) Average traces from olfactory bulb on Hit and Correct Reject (CR), averaged across mice for 9 Gad2+ and 12 VGluT1+ mice. (Means of 62 Hit, 53 CR trials per mouse for VGluT1+ and 57 Hit, 51 CR trials for Gad2+). Error bars = s.e.m.

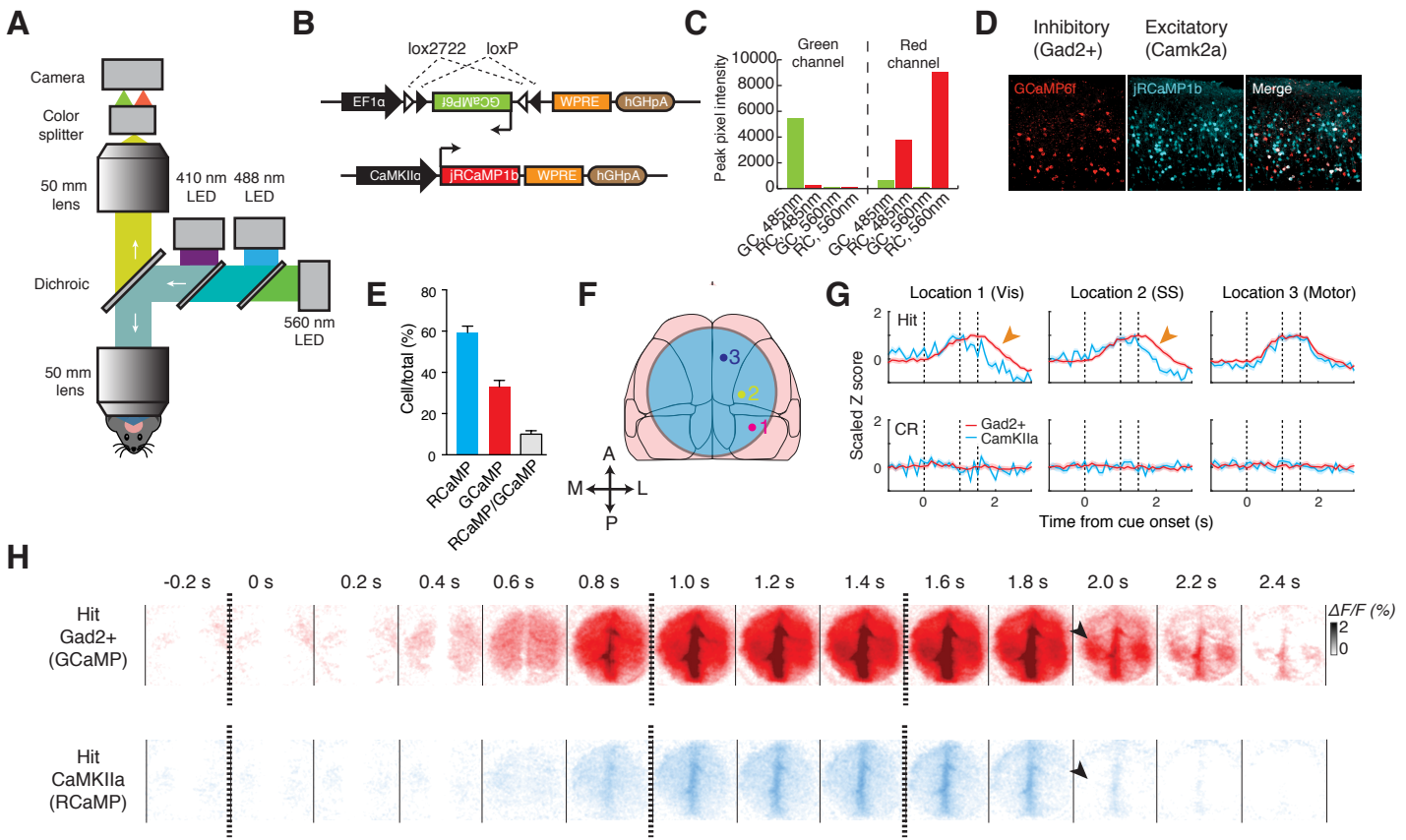


**Figure S4. Simultaneous imaging of inhibitory and excitatory dynamics during learned behavior (related to Figure 4).** (A) Dual-color macroscope schematic for simultaneous imaging of two populations of neurons. (B) Diagram of viral-genetic strategy for expression of GCaMP6f in all inhibitory neurons and jRCaMP1b in CaMKIIα-expressing (primarily excitatory) neurons. (C) Quantification of RCaMP bleed through into green channel under 485 nm illumination, and lack of GCaMP bleed through into red channel under 560 nm illumination. For this, we measured native fluorescence of fixed brain sections individually expressing either RCaMP or GCaMP in CaMKIIα expressing cortical neurons, using local AAV5 viral injection. (D) Expression of jRCaMP1b and GCaMP6f in cortex. (E) Quantification of fraction of total labeled neurons expressing jRCaMP1b, GCaMP6f, or both. (F) Diagram of 7mm window placement, and locations from which traces were extracted in next panel. (G) Average z-scored traces from three locations on Hit and Correct Reject (CR) trials, simultaneously recorded in Gad2+ and CaMKIIα populations. Mean  $\pm$  s.e.m. across n = 46 Hit, 48 CR trials in one mouse. (H) Video sequence of average fluorescence across Hit, CR trials in one mouse, simultaneously recorded. Black arrows indicate features that match those seen in Figure 4A.

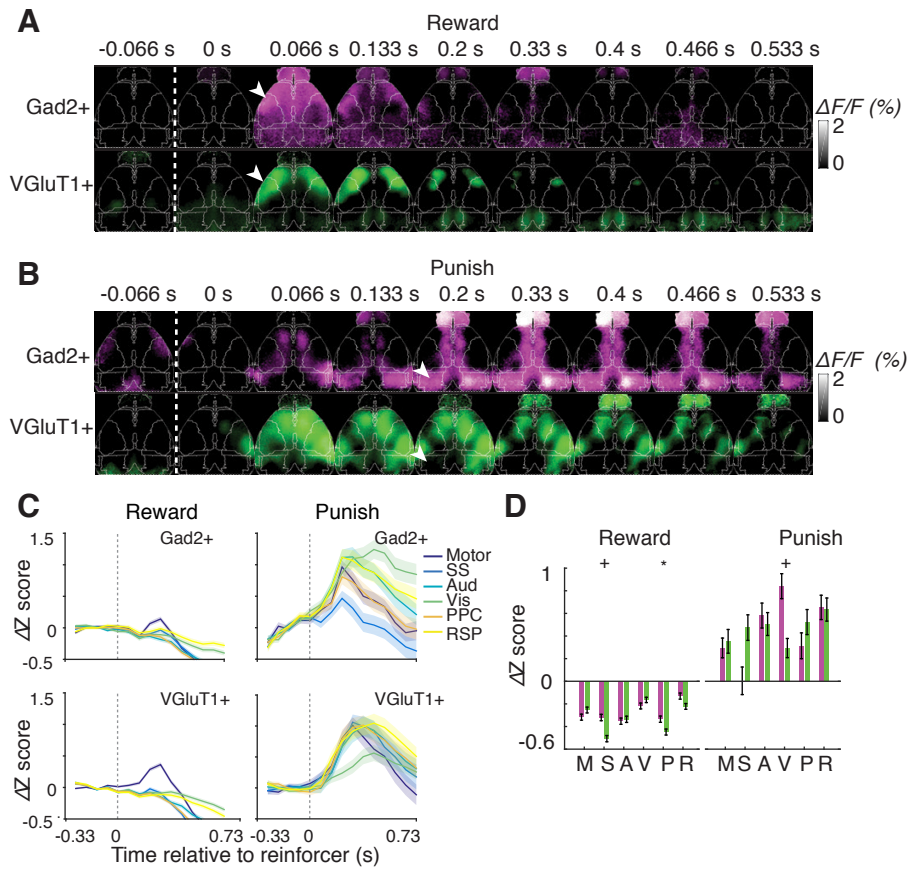


**Figure S5. Activity in response to reward or punishment (related to Figure 4).** (A-B) Specific increase in neural activity as a function of reward or punishment: Representative video sequence of average change in inhibitory or excitatory fluorescence relative to 0.33 s baseline, in response to reward (A) and punishment (B) (delivered at dotted line). Arrow in (A) indicates secondary activation of somatosensory and motor cortex as a result of reward. Arrow in (B) indicates a difference in persistent activation of visual cortex between Gad2+ and VGluT1+ following punishment. (C) Change in Z-scored fluorescence across six cortical regions, aligned to reward or punishment delivery, in Gad2+ or VGluT1+ mice. n = 362 Hit, n = 182 FA trials across N = 5 Gad2+ mice and n = 419 Hit, n = 144 FA trials N = 5 VGluT1+ mice. (D) Average values from (C) during 0.73 s after reward or punishment across six cortical regions in Gad2+ or VGluT1+ mice. M = motor, S = somatosensory, A = auditory, V = visual, P = PPC, R = RSP. \* P < 0.05, + P < 0.005, Wilcoxon rank-sum test, Bonferroni corrected. All data: mean  $\pm$  s.e.m.

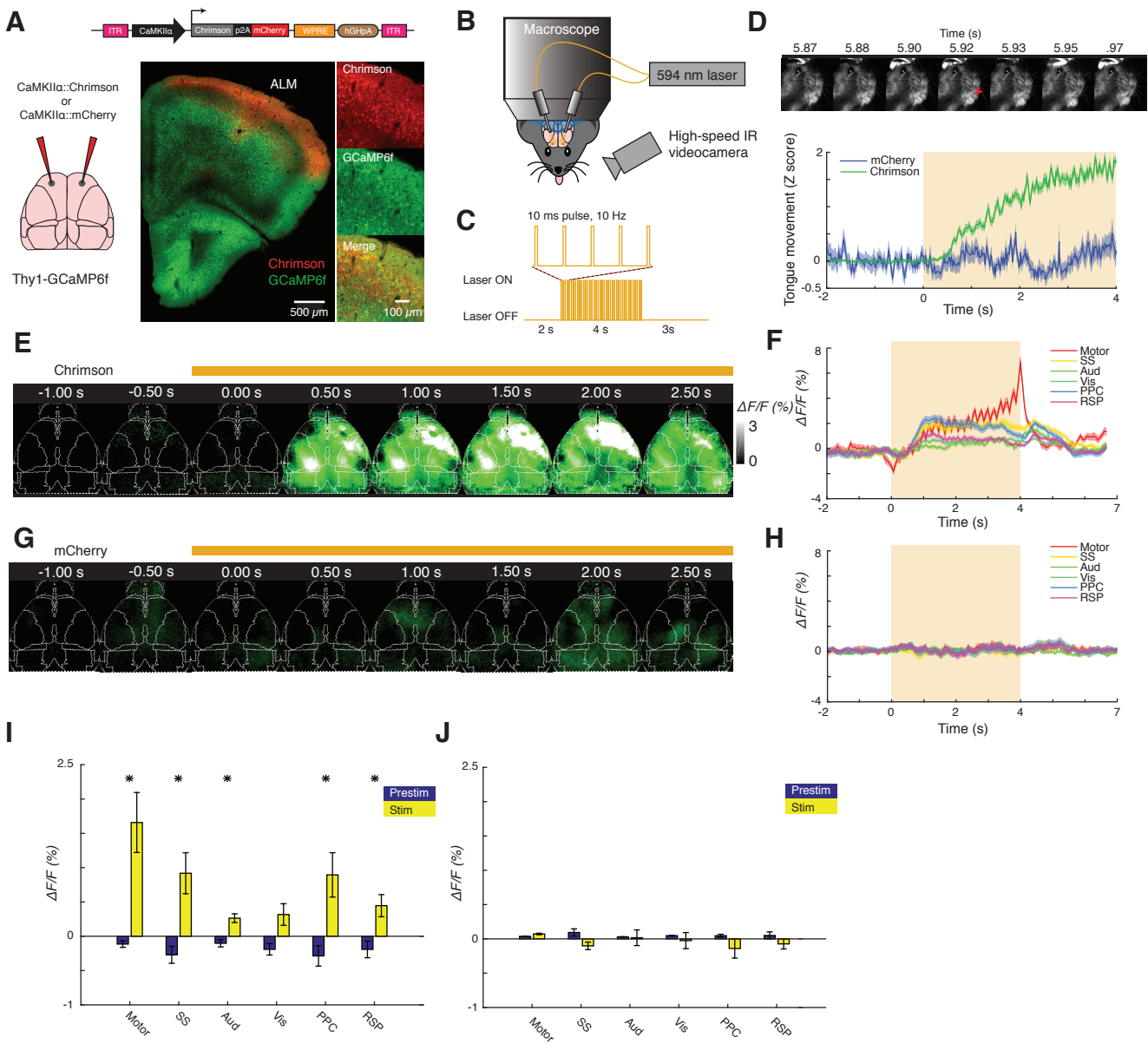


**Figure S6. Cortex-wide activation in response to optogenetic ALM stimulation (related to Figure 6).**

(A) Diagram of CaMKIIα::Chrimson-p2A-mCherry construct, diagram of injection into ALM, and expression of Chrimson-p2A-mCherry in cortex after bilaterally injection into ALM of Thy1-GCaMP6f mice. (B) Experiment schematic. Transparent skull-prepared mice were imaged with the macroscope and recorded with a high-speed infrared camera while bilaterally stimulated with fiber-coupled 594nm laser illumination projected onto ALM. (C) Stimulation and imaging parameters (10 ms on, 90 ms off), repeated for 4 s with a 2 s prestimulus period and 3 s poststimulus period. (D) Example video frames demonstrating ALM-stimulation induced licking behavior, and comparison between Chrimson-p2A-mCherry expressing mice and control mice expressing just mCherry. Red arrow indicates tongue extension from mouth. Tongue movement was quantified from video frames. (E, F) Example video sequence and regional traces of average fluorescence across time-locked stimulation trials in a Chrimson expressing mouse. Yellow bar indicates stimulation period. (G, H) Same, but for control mouse expressing just mCherry. (I) Comparison between average, across Chrimson-expressing mice, of fluorescence signal during 2 s preceding stimulation, and the period from 1 to 3 s after beginning of stimulation. \* P < 0.05, Wilcoxon rank-sum test, Bonferroni corrected, n=5 Chrimson mice. (J) Same comparison but for mCherry-expressing controls, n=2 mCherry mice. All data are presented as mean ± s.e.m.